Simulated effects of sample size and grain neighborhood on the modeling of extreme value fatigue response

Krzysztof S. Stopka 1,*, Mohammadreza Yaghoobi 2, John E. Allison 2, David L. McDowell 1,3

1 Woodruff School of Mechanical Engineering, Georgia Institute of Technology, Atlanta, GA 30332, USA.
2 Materials Science and Engineering, University of Michigan, Ann Arbor, MI 48109, USA.
3 School of Materials Science and Engineering, Georgia Institute of Technology, Atlanta GA 30332, USA.
* Corresponding author. Kstopka3@gatech.edu.

Abstract

Assessing the size of representative volume elements (RVEs) for fatigue-related applications is challenging. A RVE relevant to random microstructure requires a volume of material that is sufficiently large to capture the grain/phase heterogeneity that captures all statistical moments of the distribution of the driving force for fatigue crack formation at “hot spot” grains. Consequently, the large size of a microstructure RVE required to study fatigue phenomena is largely computationally intractable and difficult to explore. A more realistic objective in this work is to systematically study, as a function of the size of a statistical sample of microstructure, trends towards convergence of the simulated distribution of driving force for fatigue crack formation. The present work accordingly leverages the recently developed open-source PRISMS-Fatigue framework [Yaghoobi et al., npj Comput. Mater., 7, 38 (2021)] to examine the trends in convergence of extreme value distributions (EVD) of Fatigue Indicator Parameters (FIPs) in progressively larger polycrystalline microstructure realizations of FCC Al alloy 7075-T6 using crystal plasticity finite element method simulations. The results are compared to the traditional method in which ensembles of statistical volume elements (SVEs) are simulated to build up statistics intended to approximate those associated with a larger volume of material. The convergence of EVDs with increase of size of a SVE of microstructure is closely related to the extent of grain nearest neighbor (NN) interactions. Accordingly, the sensitivity of the local micromechanical response at hot spot grains is quantitatively investigated by systematically varying the orientations of NN grains. Results indicate that SVEs with cubic crystallographic texture tend towards convergence of the EVD of FIPs with tens of thousands of grains while the random and rolled textures require larger volumes. Simple relationships based on microstructure parameters (e.g., Schmid Factor, grain size, NN misorientation) do not completely correlate to fatigue hot spot grains. Finally, the sensitivity of the extreme value fatigue response at hot spot grains extends to the 3rd NN when a single neighborhood grain orientation is altered.

Keywords: fatigue; crystal plasticity; microstructure-sensitive; computational modeling; finite element method; extreme value statistics

1. Introduction

Crystal plasticity finite element method (CPFEM) simulations are ubiquitous in studies of polycrystalline metal deformation, texture development, and low probability life-limiting events such as fatigue crack formation [1-3]. The latter requires a sufficient volume of simulated material to capture statistics of a larger ensemble of grain/phase heterogeneity. Instead of simulating a single, large representative volume element (RVE), statistical volume elements (SVEs) are multiple samples of microstructure that can be simulated as an ensemble to establish statistics of response as a concession to the high computational cost for simulation of a single large RVE [3]. The size of a RVE must be sufficiently large to contain all statistical moments of heterogeneous grain/phase spatial interactions that affect a target material property irrespective of boundary conditions [4, 5] and, therefore, will not vary with increased volume of the microstructural ensemble considered, i.e., RVE size. The convergence of elastic properties (e.g., elastic stiffness) typically requires the least volume of material, i.e., the smallest RVE, whereas properties that depend on plastic flow response (e.g., yield strength, cyclic stress-strain curve) require larger volumes and associated RVEs. The RVE size is particularly large for local extreme value fields such as driving forces to form fatigue cracks in hot spot grains. In this case, the RVE must be large enough to sufficiently sample all possible grain orientation space and interactions amongst neighboring grains, which can be inordinately large. From a practical perspective, even the existence of a RVE for fatigue is a challenging issue to assess, since laboratory fatigue experiments invariably exhibit scatter at all specimen sizes considered, as do engineering components that fail via fatigue. Moreover, beyond randomness of microstructure, the issue of a RVE for fatigue response as measured via laboratory experiments includes effects of environment and surface condition that may not be considered in computational simulations. Even if the RVE size for extreme value driving forces to form and grow fatigue cracks cannot be fully resolved, some sense of the rate of convergence of theses extreme value driving forces with increases in the size of the highly stressed volume of microstructure is quite relevant to fatigue modeling. This is the primary thrust of the current paper.

Let us consider polycrystalline materials. Several researchers have previously explored RVE size for certain behaviors of polycrystalline materials. Qayyum et al. [6] simulated the global and local stress-strain response in progressively larger 2D and 3D RVE microstructures of single- and dual-phase steels. They concluded that 3D RVEs for this response must be at least five times larger than the average grain size. They later incorporated an isotropic ductile damage model based on the total accumulated plastic slip to assess differences in damage initiation for 2D and 3D RVEs [7]. Bong et al. [8] investigated a

bottom-up method to generate a RVE for dual phase steel DP980 using measured microstructural properties. Mechanical behavior was then determined using a standard continuum model, a CPFEM model, and a CPFEM model that included elastic interactions of discrete dislocations in the martensite and ferrite phases. The latter model better predicted strain hardening behavior and matched loading-unloading and compression-tension experiments. Bouchedjra et al. [9] estimated the RVE size for convergence of macroscopic elastoplastic behavior in Al alloy 5083 with several microstructure realizations ranging from 10 to 250 grains. The elastoplastic and local response of different FCC RVE single crystals and polycrystalline microstructures was examined by Lim et al. [10] using various mesh resolutions, boundary conditions, and hardening models. Tu et al. [11] developed a workflow to generate statistically equivalent representative volume elements (SERVE) of Al alloy 7075-T651 that considered morphological and crystallographic distribution of grains and the presence of precipitates. They determined the minimum number of grains for microstructure-based and property-based SERVEs, having distinguished between these. The former corresponds to the minimum size at which the statistics of any crystallographic or morphological feature in the digital microstructure converges to that of the experimental data, whereas the latter corresponds to the minimum size that should be analyzed to predict some effective material property of interest. Sangid et al. [12] combined high energy x-ray diffraction microscopy (HEDM) and digital image correlation (DIC) coupled with electron backscatter diffraction (EBSD) to examine the stress-strain response of individual grains in Ni-base superalloy Haynes 282 and Ti alloy Ti-7Al. The number of sampled grains necessary to constitute a RVE was determined using grain-level variability and was higher for Haynes 282 because of its larger grain size distribution, underlying precipitate structure, and the presence of annealing twins. Ozturk et al. [13] studied the convergence of elastic stress and strain fields in Ni-based low solvus high refractory (LSHR) superalloy using experimentally reconstructed and synthetic microstructures. The comprehensive review by Bargmann et al. [14] systematically classified the 3D RVE generation corresponding to specific responses for several heterogeneous engineering materials of interest.

As previously mentioned, the present work considers the maximum driving force for fatigue crack formation as the response of interest. Fatigue Indicator Parameters (FIPs) serve as surrogate measures of the driving force for fatigue crack formation [3, 15] and can capture the effects of intrinsic and extrinsic microstructure properties (e.g., grain size [16] and morphology [17], crystallographic texture [17], surface roughness [18, 19], presence of inclusions [20], porosity [21], etc.) and loading conditions (e.g., applied strain state and magnitude [22]). FIPs can be related to experimentally measured fatigue life using an appropriate calibration process [16]. The Fatemi-Socie FIP has been

shown to correlate well with the transgranular fatigue crack formation driving force [23]. Other common FIPs include a grain boundary impingement FIP that considers the irreversible plastic shear strain accumulated at a grain boundary and the peak stress normal to this boundary [24], stored energy density [25], and a combination of the maximum local resolved shear stress and the peak hydrostatic stress [18]. To circumvent expensive CPFEM simulations, strategies have been developed to predict the extreme value response of larger microstructure SVEs. Stopka, Gu, and colleagues [26, 27] used extreme value theory to extrapolate FIPs to larger volumes of Ti alloy Ti-6Al-4V based on extreme value FIPs assessed using a limited number of simulated SVEs. A similar framework was developed by Lucarini and Segurado [28] using a crystal plasticity model of Ni-base superalloy IN 718 implemented into a Fast Fourier Transform (FFT) solver. Both methods require calibration and may be sensitive to material system, constitutive model employed, etc.

Interactions between nearest neighbor (NN) grains critically affect the local fatigue response and directly influence the RVE size for fatigue related applications. Boyle and Curtin [29] investigated how the strain in a central grain of interest deviates from the global applied strain in an FCC material when i) the orientation of the grain of interest (GOI) is changed, ii) the orientations of the first NN grains are changed, and iii) the orientations of the second NN grains are changed. The microstructure instantiation was composed of cubic geometry grains with 343 grains in a 7 x 7 x 7 array. Each grain was then discretized with 1, 8, or 27 elements. They showed that for most of the tested configurations, deviations from the applied strain are primarily influenced by interactions with the surrounding grain environment, and not by the orientation of individual GOIs. Castelluccio and McDowell [30] similarly investigated FIP variability in a surface grain by altering the orientations of NN grains in FCC Ni-base superalloy RR1000. They also held the orientation of the GOI and orientations of the first NN grains constant and changed all other grain orientations (second NN grains and beyond). Grain interactions in the first NN grain layer affected variability of the maximum FIP by a factor of 2-3, while the orientations of second NN grains and beyond accounted for ~30% of the variability. In a recent work on dual-phase steels, Diehl et al. [31] compared the local stress-strain response at free surface grains after varying grain orientation, grain morphology, and volume fraction of two hard and soft phases in subsurface grains. Structural changes farther than about three average grain sizes were considered negligible for stress and strain partitioning. Variations in grain morphology and an increase in microstructure heterogeneity more strongly affected the local stress-strain response at the surface grains than changes in grain orientations. They also found that the assumption of a columnar grain structure introduces a strong simplification that may be misleading in 2D simulations of damage in 3D microstructures.

Dunne, Rugg, and Walker [32-34] introduced the concept of a rogue grain combination in high strength HCP Ti alloys, in which a primary grain is oriented with its c-axis at or near parallel to the loading direction (i.e., grain in a “hard” orientation) with adjacent grains oriented for easy slip on basal or prismatic slip systems (i.e., grains in “soft” orientations). These hard-soft grain combinations under cold-dwell fatigue loading are thought to result in fatigue facet nucleation. Interestingly, the effect of altering the grain orientation of a soft grain was limited to its first NN grains [32]. This has recently been highlighted as a significant difference between the local response of FCC and HCP alloys under fatigue loading [17]. Sauzay and Jourdan [35] examined the elastic response of a surface grain surrounded by NN grains with different FCC elastic anisotropies (aluminum, ferrite, copper, and austenite) and simulated under different loading conditions (tension-compression, equibiaxial, and shear loading). Random orientations for the NN grains were selected 60 times and finite element computations were used to quantify scatter in the stress of the well-oriented slip system in the surface grain. They also simulated grains in hard and soft orientations as described above to quantify the extreme value responses with a reduced computational cost [35].

Let us consider a primary GOI. A hard grain positioned along the loading direction or a soft grain positioned transverse to the loading direction both enhance stress in the GOI. In contrast, a soft grain along the loading direction or a hard grain in the transverse direction diminish the stress in the GOI [36, 37]. Abdolvand et al. [38] studied these critical grain combinations in commercially pure Zr and Ti. Samples were strained with in situ HEDM measurements to determine center of mass, average elastic strain, stress, and lattice orientation, and relative volume of each grain in the scanned volume. Digital microstructures using HEDM data were then reconstructed for CPFEM simulations. They found that grain-grain interactions had a significant effect on stress relaxation by simulating the reconstructed sample with different scenarios: i) lattice rotations disabled, ii) new random orientations assigned to grains with the same grain shapes and positions, and iii) simulating a new synthetic microstructure instantiation where each grain was represented by a single element [38]. Kawano et al. [37] formulated a metric called slip operation factor (SOF) to predict plastic slip in HCP α-Ti based on the Schmid Factor of a grain, the Schmid Factors of several NN grains, the critically resolved shear stress, and a spatial weight function. They later extended this method to consider individual and secondary slip systems [36]. Harte et al. [39] used EBSD and high-resolution DIC to measure plastic strain in Ni-based superalloy RR1000 strained to 2%. They found a weak correlation between grain plasticity and grain orientation derived metrics such as the Schmid Factor or Taylor Factor due to deformation bands at the mesoscale that were not crystallographic and complex interactions between grains. Musinski et al. [40] arrived at a

similar conclusion for Ni-based LSHR superalloy. Harte et al. [39] concluded that the use of the Schmid Factor and the concept of “hard” and “soft” grains may be appropriate for plastic deformation analysis in more anisotropic materials (e.g., HCP Ti alloys as described above), but that these are not as relevant to FCC γ/γ’ Ni-based superalloys at small global plastic deformation.

Increases in computational resources and algorithm efficiency now allow for massive CPFEM simulations to evaluate the micromechanical response of polycrystalline metals and alloys. These tools can be used to evaluate distributions of fatigue parameters over large statistical volume elements of microstructure, defined earlier as SVEs. The recently developed open-source PRISMS-Fatigue framework can generate very large SVEs of microstructure, perform CPFEM simulations, and compute volume-averaged FIPs [41]. PRISMS-Fatigue is a highly efficient, flexible, scalable, and easy-to-use Integrated Computational Materials Engineering (ICME) community platform. It is a component of the Center for PRedictive Integrated Structural Materials Science (PRISMS Center) suite of high performance open-source software [42] and uses PRISMS-Plasticity as its CPFEM engine [1, 43, 44]. Furthermore, it is linked to the Materials Commons [45] to record simulations and workflows and to publish and share data with collaborators.

The goal of this article is to leverage the advanced capabilities of PRISMS-Fatigue to employ CPFEM to evaluate FIP characteristics in very large polycrystalline microstructure SVEs of FCC Al alloy 7075-T6 and to consider how the associated extreme value distributions (EVDs) of FIPs may converge with increase of SVE size, which would point to an approach towards RVE response. More specifically, one of the goals is to determine whether progressively larger microstructure SVEs manifest FIP EVDs with gradually larger magnitudes, and to investigate the structural characteristics or spatial correlations of hot spot grains that manifest the highest FIPs. Subsequently, a systematic study on the largest SVE investigates the influence of NN grain interactions on the extreme value FIPs. We emphasize that this type of design of experiments (i.e., altering the grain neighborhood at fatigue hot spots) is straightforward to implement in this type of computational study but is much more challenging (if not impossible) to pursue in physical experiments. Section 2 reviews the crystal plasticity model, generation of digital microstructure SVEs, calculation of FIPs, and extreme value statistics. Section 3 then investigates the combined effects of crystallographic texture, grain morphology, and different sized SVEs on the extreme value fatigue response. Progressively larger SVEs with the same target number of grains are simulated in Section 4, the largest of which contains over 160,000 grains discretized by a 2503 = ~15.6 million finite element mesh. The structural characteristics of the ~5-10 highest FIPs in the

~160,000 grain SVE are then investigated, specifically whether the concept of “hard” and “soft” grains is relevant to fatigue hot spots in this material system. Section 5 quantifies the effects of NN grains on the extreme value FIPs in the ~160,000 grain SVE. Section 6 provides a discussion of the results, and we draw conclusions in Section 7.

2. Methodology

This section describes the tools used in this study. The crystal plasticity constitutive model and digital microstructure SVE generator are first reviewed. The use of FIPs as surrogate measures for the driving force for fatigue crack formation and their volume averaging scheme is described next. Finally, extreme value statistics are reviewed.

2.1. Crystal plasticity model

The rate-dependent crystal plasticity model implemented in PRISMS-Plasticity [1, 41, 46] is employed here to calculate FIPs. The model can capture both isotropic and kinematic hardening. The deformation gradient tensor $\mathbf{F}$ is multiplicatively decomposed as

$$\mathbf{F} = \mathbf{F}^{\mathrm{e}}\mathbf{F}^{\mathrm{p}} \tag{1}$$

where $\mathbf{F}^{\mathrm{e}}$ and $\mathbf{F}^{\mathrm{p}}$ are the elastic and plastic deformation gradient tensors, respectively. Next, the macroscopic velocity gradient tensor $\mathbf{L}$ is additively decomposed as

$$\mathbf{L} = \mathbf{L}^{\mathrm{e}} + \mathbf{L}^{\mathrm{p}} \tag{2}$$

where $\mathbf{L}^{e}$ and $\mathbf{L}^{\mathrm{p}}$ are the elastic and plastic velocity gradient tensors, respectively. The plastic velocity gradient tensor can be obtained by compiling the shearing rates of different slip systems, i.e.,

$$\mathbf{L}^{\mathrm{p}} = \dot{\mathbf{F}}^{\mathbf{p}}\mathbf{F}^{\mathbf{p}-1} = \sum_{\alpha=1}^{n_s} \dot{\gamma}^{\alpha}\mathbf{S}^{\alpha} \tag{3}$$

Here, $\dot{\gamma}^{\alpha}$ is the shearing rate on the α^{th} system, n_s is the number of slip systems, and $\mathbf{S}^{\alpha}$ is the Schmid tensor for the slip system α in the intermediate configuration defined by

$$\mathbf{S}^{\alpha} = \mathbf{m}^{\alpha} \otimes \mathbf{n}^{\alpha} \tag{4}$$

where unit vectors $\mathbf{m}^{\alpha}$ and $\mathbf{n}^{\alpha}$ are in the slip direction and slip plane normal direction, respectively, for slip system α in the intermediate isoclinic configuration.

The flow rule in the rate-dependent crystal plasticity model is given by

$$\dot{\gamma}^{\alpha} = \dot{\gamma}_0 \left| \frac{\tau^{\alpha} - \chi^{\alpha}}{s^{\alpha}} \right|^{m} \operatorname{sgn}(\tau^{\alpha} - \chi^{\alpha}) \tag{5}$$

where $\dot{\gamma}_0$ is the reference shearing rate, m is the inverse strain rate sensitivity exponent, τ^{α} is the resolved shear stress for slip system α, and s^{α} and χ^{α} are the slip resistance and back stress of the slip system α, respectively.

Isotropic hardening via the slip resistance is assumed to follow

$$\dot{s}^{\alpha} = \sum_{\beta} h^{\alpha\beta} \dot{\gamma}^{\beta} \tag{6}$$

where $h^{\alpha\beta}$ are the hardening moduli which control the change in the slip resistance for slip system α by virtue of slip on system β. The hardening moduli $h^{\alpha\beta}$ are defined using a power-law relationship [47], i.e.,

$$h^{\alpha\beta} = \begin{cases} h_0^{\beta} \left[1 - \dfrac{s^{\beta}}{s_s^{\beta}} \right]^{a^{\beta}} & \text{if} \quad \alpha = \beta \text{ (coplanar systems)} \\ h_0^{\beta} q \left[1 - \dfrac{s^{\beta}}{s_s^{\beta}} \right]^{a^{\beta}} & \text{if} \quad \alpha \neq \beta \end{cases} \tag{7}$$

Here, q is the latent hardening ratio, h_0^{β} denotes the hardening parameter for slip system β, s_s^{β} is the slip resistance at hardening saturation for slip system β, and a^{β} is a material constant for slip system β which governs the sensitivity of the hardening moduli to the slip resistance.

The kinematic hardening in the crystal plasticity model is assigned using a two-term Ohno-Wang type evolution law, i.e.,

$$\dot{\chi}_i^{\alpha} = h_i \dot{\gamma}^{\alpha} - r_i \left(\frac{|\chi_i^{\alpha}|}{b_i} \right)^{m_i} \chi_i^{\alpha} |\dot{\gamma}^{\alpha}|, \qquad \dot{\chi}^{\alpha} = \sum_{i=1}^{2} \dot{\chi}_i^{\alpha} \tag{8}$$

where r_i and h_i are material constants, and the variables $b_i = {}^{h_i}/_{r_i}$, and m_i control the dynamic recovery. Note that Eq. (8) reduces to the Armstrong-Frederick back stress formulation in the case of

$m_i = 0$. The two-term back stress formulation in Eq. (8) decouples the back stress response into short- and long- range components that are necessary for appropriate model calibration [48].

The material model parameters were calibrated by Hennessey et al. [48] for the cyclic response of Al 7075-T6 alloy using fully reversed quasi-static cyclic stress-strain data at strain amplitudes of 1.0% and 1.8% at room temperature. Hennessey et al. [48] used experimental peak stress-plastic strain response data to calibrate the model. The only difference in the model employed here are the values of m1 and m2, which are selected as 70 instead of 200 [41]. The hardening in the current work is assumed to be purely kinematic to capture the cyclically stable response of Al 7075-T6 alloy, i.e., isotropic hardening is not considered. Precipitates in this material system are not explicitly represented in the model or microstructure SVEs but they were implicitly considered in model parameter calibration by Hennessey et al. [48]. The elastic constants are $C_{11} = 107.3$ GPa, $C_{12} = 60.9$ GPa, and $C_{44} = 28.3$ GPa [41, 48]. A reference shearing rate of $\dot{\gamma}_0 = 0.001\ s^{-1}$ and an inverse strain rate sensitivity of $m = 75$ were used in all simulations. Model parameters are summarized in Table 1.

Table 1. The material model parameters for the Al 7075-T6 crystal plasticity model.

m	s^{α} (MPa)	h_1 (MPa)	r_1	h_2 (MPa)	r_2	$m_1 = m_2$
75	35	2×10^6	2×10^4	1.35×10^5	1421	70

The crystal plasticity model and consequently the fatigue analysis cannot capture the effects of grain size and grain boundary-mediated slip transfer. To address grain size effects, one can use strain gradient models [49, 50]. Furthermore, the isotropic and kinematic hardening models used in the current model are phenomenological. These can be enhanced by incorporating dislocation density-based hardening laws [49]. The focus of the current work is on the effect of statistical ensemble size and grain neighborhood for fatigue analysis, whereas the effect of grain size and physically-based hardening laws can be incorporated as a future study.

2.2. DREAM.3D microstructure SVE generation

Microstructure SVEs are generated using the open-source DREAM.3D software [51]. The methodology outlined by Groeber et al. [52, 53] to first statistically characterize polycrystalline materials

using EBSD and serial-sectioning [52] and then to digitally reconstruct the samples for simulation [53] led to the development of DREAM.3D. It is commonly used to generate synthetic microstructure SVEs for subsequent simulation but can also reconstruct experimental microstructures using grain centroids and relative volumes from HEDM experiments [54, 55], and use statistics from these reconstructions to generate statistically equivalent microstructures [56]. The Python module entitled generate_microstructures.py in PRISMS-Fatigue calls DREAM.3D as a subprocess to generate the microstructure SVEs and create the necessary files for PRISMS-Plasticity CPFEM simulations and subsequent FIP calculations.

Periodic microstructure SVEs are generated to accord with the periodic boundary conditions applied in the CPFEM simulations, which are described in the next section. Grain size follows a lognormal distribution with a mean and standard deviation of 14 µm ± 2 µm. The combined effects of grain morphology, crystallographic texture, and the number of grains simulated on the extreme value fatigue response are studied in this work. The smallest SVEs simulated contain ~250 grains represented by 293 voxels and are shown in Fig. 1a and Fig. 1b for equiaxed and elongated grain morphologies, respectively. Grains are elongated in the X direction with a ratio of 5:1:1 to represent cold-rolled morphology [17, 57]. Both grain morphologies result in the same nominal number of grains per SVE [17]. Three common crystallographic textures are examined with orientation distribution function (ODF) pole figures shown in Fig. 1. These include cubic (observed after recrystallization or homogenization heat treatment [58]), random, and rolled (observed after cold rolling [59]).

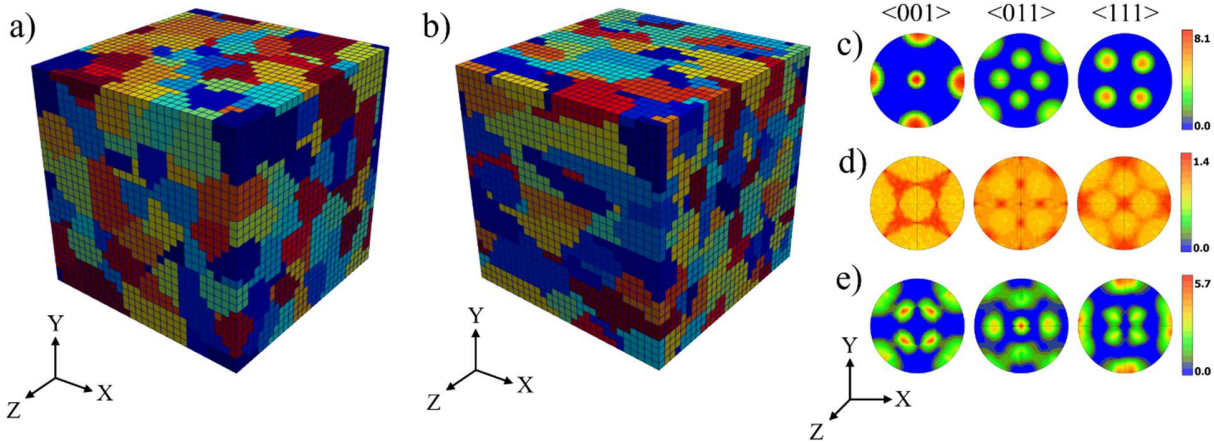

Fig. 1. Sample 293-element microstructure statistical volume elements (SVEs) with a) equiaxed and b) elongated grain morphology. In the latter, grains are elongated in the X direction with the ratio 5:1:1 [17, 57]. Orientation distribution function (ODF) pole figures for the c) cubic (observed after

recrystallization or homogenization heat treatment [58]), d) random, and e) rolled (observed after cold rolling [59]) crystallographic textures [41].

2.3. Boundary and loading conditions

Periodic boundary conditions are imposed in all three directions using multi-point constraints for all SVEs of microstructures simulated in this work. The efficacy of these constraints was previously investigated and shown to work well to emulate bulk, subsurface material response [60]. Previous computational studies have extensively investigated the surface vs. subsurface effect on the extreme value fatigue response of SVEs [17, 41, 60]. The goal of this work is to evaluate the effects of sample size and grain neighborhood; accordingly, all simulations employ periodic boundary conditions to exclude surface effects.

All simulations undergo fully reversed ($R\varepsilon = -1$) uniaxial cyclic straining to a strain amplitude of 0.7% (representative of high cycle fatigue (HCF) loading with limited macroscopic plastic strain) with zero initial strain and back stress. Straining is initiated in compression and reduced integration elements are employed. Two cycles are applied after which FIPs are computed for each integration point and volume averaged over a complete loading cycle. Local variables rapidly saturate using the crystal plasticity model employed and so further cycling is not warranted. The convergence of FIPs after two cycles for a single microstructure SVE is shown in the supplementary information. Additionally, the largest microstructure SVE simulated in this work contains $2503 = 15{,}625{,}000$ elements, which is quite computationally demanding. All SVEs are uniaxially strained in the X direction as shown in Fig. 1a and Fig. 1b, i.e., SVEs with elongated grain morphology are uniaxially strained in the direction of grain elongation. SVEs are also strained in the X direction relative to the crystallographic ODF pole figures shown in Fig. 1c-e.

2.4. Fatigue Modeling and Fatigue Indicator Parameters

For HCF experiments on polycrystalline metals, the early stages of fatigue crack formation and growth are strongly influenced by the microstructure [3, 61]. Crack formation is very complex since the crack size is comparable to the grain size at initial stages of fatigue life. Accordingly, microstructure features as well as the deformation mechanisms within grains and interactions of grain boundaries (GBs)

with the small fatigue cracks are important [61]. We may consider crack formation in HCF to be comprised of crack nucleation plus early growth to a size comparable to the grain size. In the case of HCF, the crack formation phase is a significant fraction of the sample lifetime. Accordingly, the HCF life is strongly influenced by its microstructure. This leads to both strong dependence of mean fatigue lifetime on microstructure, as well as large variability of lifetime in the HCF regime.

For purposes of computational simulation of estimated driving force, we employ FIPs as computable quantities of interest within individual grains/subgrain regions [3]. FIPs serve as surrogate measures for the driving force for fatigue crack formation. Many FIPs and fatigue damage parameters have been introduced and evaluated over the last two decades [3]. Fatemi and Socie [62] considered the maximum plastic shear strain range on a plane and the peak stress normal to this plane in their FIP definition. A crystallographic version of the Fatemi-Socie FIP is employed in this work, i.e.,

$$FIP_{\alpha} = \frac{\Delta\gamma_p^{\alpha}}{2}\left[1 + k\frac{\sigma_n^{\alpha}}{\sigma_y}\right] \tag{9}$$

where $\Delta\gamma_p^{\alpha}$ is the range of cyclic plastic shear strain on the αth slip system, σ_n^{α} is the peak stress normal to this slip plane, and k controls the influence of σ_n^{α} which is normalized by the macroscopic yield strength σ_y [23]. k and σ_y are set to 10 and 517 MPa, respectively [17, 22]. Stopka and McDowell [22] recently reviewed a series of FIP formulations. Bozek, Hochhalter, and colleagues [63-65] established a framework to investigate fatigue crack incubation at constituent particles and subsequent nucleation to the surrounding matrix in aluminum alloy 7075-T651. They demonstrated that slip-based metrics computed over appropriate domains could determine which incubated cracks nucleate. FIPα (herein referred to simply as FIP) is employed here as an exemplar of a surrogate driving force for fatigue crack formation to facilitate computational exploration of extreme value fatigue response of large microstructure SVEs.

FIPs are computed for each integration point and must be subsequently volume averaged over a defined volume for two primary reasons: (1) to reflect the fatigue damage process zone (since fatigue cracks form over some volume and not at a point) and (2) to mitigate the effects of mesh sensitivity [3]. Selection of the defined volume requires careful consideration. FIPs averaged over the entire grain are computationally the least demanding but the variation in grain size means that FIPs are averaged over different volumes which may skew the interpretation of the data. Additionally, fatigue crack formation occurs within a damage process zone at sub-grain scales on the order of up a few microns and not across an entire grain/phase, although it may or may not propagate rapidly across this grain/phase.

Thus, averaging of FIPs over entire grains may smear extreme FIP values in hot spot regions of the grain and underestimate the actual driving force.

Castelluccio and McDowell [16, 30] introduced the concept of grain banding in which the elements of a grain are divided into slip bands that are parallel to crystallographic slip planes (see Fig. 5a in Ref [41]). FIPs can then be averaged over these bands that accord with experimentally observed transgranular fatigue crack formation and early growth on crystallographic slip planes and serve to mitigate mesh sensitivity. Stopka and McDowell further subdivided these bands into sub-bands to hold the averaging volume constant [17, 22]. In this work, FIPs are averaged over these sub-bands to provide a regularized averaging scheme (Fig. 5b in Ref [41]). Other researchers have recently developed other volume averaging schemes for fatigue metrics [21, 66]. The Python module calculate_FIPs.py in PRISMS-Fatigue allows the user to choose from a library of FIPs. The volume_average_FIPs.py module then allows the user to volume average FIPs over grains, bands, or sub-bands. Stopka et al. [27] previously investigated the effect of different sub-band averaging volumes on FIP EVDs.

2.5. Extreme value statistics of FIPs

After FIPs are computed and volume averaged, the highest values are fit to the Gumbel EVD. Distributions of a single variable with a sufficiently large sample size n will converge to one of three non-degenerate distributions: 1) Gumbel, 2) Fréchet, and 3) Weibull [67]. The latter requires an upper bound on the data and is therefore not considered. FIPs have previously been characterized well by both former distributions with subtle difference depending on whether fully periodic or “thin film” boundary conditions were prescribed [68]. FIPs are fit to the Gumbel EVD in this work which is expressed as

$$F_{Y_n}(y_n) = exp\left[-e^{-\alpha_n(y_n-u_n)}\right] \tag{10}$$

where $\mathrm{F_{Y_n}(y_n)}$ is the probability that the value $\mathrm{Y_n}$ will be less than or equal to $\mathrm{y_n}$, $\mathrm{u_n}$ is the characteristic largest value of the sampled population, and $\mathrm{\alpha_n}$ is an inverse measure of dispersion of the largest value of the population [67]. FIPs are sorted in ascending order and their probabilities are estimated by

$$F_{Y_j}(y_j) = \frac{j-0.3}{n+0.4} \tag{11}$$

where j is the rank order of the corresponding FIP, and n is the number of FIPs from a single or multiple SVEs. Eq. (11) is written as a linear function of y in the form

$$ln\left[ln\left(\frac{1}{F_{Y_n}(y_n)}\right)\right]^{-1} = \alpha_n y_n - \alpha_n u_n \quad (12)$$

where α_n is the slope and $-\alpha_n u_n$ is the y-intercept. In this mathematical form, data that are well characterized by a Gumbel distribution appear as a straight line. Only a single sub-band volume averaged FIP is considered per grain. Gu et al. [26] examined the convergence behavior of FIPs fit to the Gumbel EVD and devised a strategy to predict the maximum FIPs in larger volumes using extreme value theory. This requires a rigorous consideration of a FIP threshold in the fitting process. In this work, some number of the highest FIPs (either 50 or 100, depending on the total number of grains simulated) from each SVE or SVE ensemble are fit to the Gumbel EVD for the sole purpose of rank ordering relative fatigue resistance, i.e., only the highest FIPs are of interest since these are associated with the highest driving forces for fatigue crack formation. The Python module entitled compile_and_plot_FIPs.py in PRISMS-Fatigue performs these tasks and allows the user to fit FIPs to either the Gumbel or Fréchet EVD.

3. Crystallographic texture and grain morphology effects on FIP EVDs

The effects of crystallographic texture and grain morphology on the convergence of FIPs are investigated using two different scenarios for a given microstructure:

- The FIP EVDs for an ensemble of smaller SVEs are compared to the FIP EVDs of a single large microstructure SVE that contains the same total number of grains as the ensemble
- FIP EVDs for progressively larger SVEs with many more grains are compared

Three microstructure SVE sets are generated and simulated for each combination of texture and morphology. The first set is an ensemble of 30 SVEs each with 293 elements and ~250 grains, and therefore a total of ~7,500 grains. The second set is a single, larger SVE for the same statistical target microstructure with 903 elements and the same total of ~7,500 grains. The third set is also a single but much larger SVE with 1603 elements and ~41,000 grains, and therefore more than five times the volume and grains of the two previous SVEs. The first, second, and third sets contain (30 x 6) = 150, 6, and 6 microstructure SVE realizations, respectively, which are subjected to fully reversed uniaxial cyclic straining at a strain amplitude of 0.7% as described in Section 2.3.

The macroscopic cyclic stress-strain response of the SVEs in this section does not vary with the number of grains simulated (see supplementary Fig. S2). The cubic texture manifests a slightly softer

response since plastic deformation is, on average, more homogeneously distributed. The macroscopic response is also unaffected by grain morphology, but it is important to note that the SVEs here are strained in the direction of grain elongation. The macroscale response of SVEs with as little as ~250 and many as ~160,000 grains were previously shown to be indistinguishable (see Fig. 3e in [41]). Thus, the RVE size for macroscale stress-strain response is readily achieved, but this is not the case for the microscale response or FIP hot spots. The latter will be discussed in the next subsection while the former is investigated below.

The cumulative effective plastic strain, defined as $\varepsilon_{CEP} = \int \sqrt{\frac{2}{3}\dot{\boldsymbol{\varepsilon}}^p : \dot{\boldsymbol{\varepsilon}}^p}\, dt$ where $\boldsymbol{\varepsilon}^p$ is the plastic strain tensor, is extracted from each voxel at the conclusion of the simulations and is shown in Fig. 2 for the second and third microstructure SVE sets depicted in Fig. 3b and Fig. 3c. We previously showed that distributions of ε_{CEP} from SVEs of the same target microstructure follow similar trends but are not identical [60], and so identical responses are not expected between the different-sized SVEs of a given crystallographic texture and grain morphology. The distributions differ mainly due to texture with little effect due to SVE size and grain morphology. The ε_{CEP} is more homogenously distributed in the cubic texture with no voxels exhibiting particularly low or high values while the random and rolled texture distributions are broader and lead to fatigue hot spots that are investigated next.

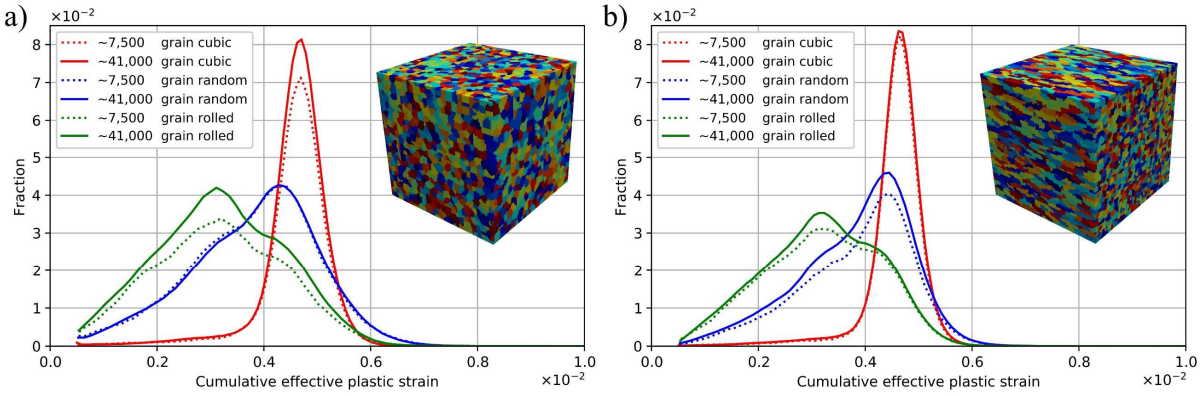

Fig. 2. Distributions of cumulative effective plastic strain (ε_{CEP}) for the second and third microstructure SVE sets of Section 3 for the a) equiaxed and b) elongated grain morphology. The ε_{CEP} is extracted from each voxel at the conclusion of the simulations. The Y axis shows the fraction of data at each value of ε_{CEP} since the ~7,500 grain and ~41,000 grain SVEs differ in number of voxels (i.e., 903 and 1603 voxels, respectively).

3.1. Smaller SVE ensemble response versus a single large SVE

FIPs are computed for each SVE in the first set of an ensemble of smaller SVEs and compiled, after which only the highest 50 are considered. In the second and third cases (Fig. 3b and Fig. 3c), the highest 50 FIPs from each single larger SVE are considered. The first comparison is made between FIP EVDs for the same nominal number of simulated grains from an ensemble of smaller SVEs and a single large SVE, as shown in Fig. 3a and Fig. 3b, respectively. This comparison permits the rank ordering of relative fatigue resistance between the six different combinations of crystallographic texture and grain morphology. The variability in the extreme value FIP for multiple microstructure realizations of the same target microstructure and sample size will be investigated later. The six data sets from both scenarios are comparable and FIP rank ordering is unchanged. The axis limits are identical in all figures to facilitate straightforward comparison. The FIPs for the cubic textured microstructure show the highest resistance to fatigue (i.e., the lowest FIPs) whereas the rolled texture with equiaxed grain morphology displays the highest FIPs and therefore least resistance to fatigue. As will be demonstrated later, simulating a limited number of grains (e.g., ~7,500) is insufficient to constitute a RVE for EV FIPs. In other words, different realizations of a single large SVE or SVE ensembles may result in substantial variability amongst FIP EVDs. However, a limited number of simulated grains, namely EV FIPs from an ensemble of smaller SVEs, may suffice for rank-ordering of fatigue resistance; this is clearly indicated by comparing Fig. 3a and Fig. 3b to Fig. 3c. An interesting observation is that the elongated grain morphology reduces extreme value FIPs, which is most likely a consequence of plastic shear strain constraints due to the reduced mean free slip path. It is expected that cyclic straining in another direction, perhaps perpendicular or at 45° to the elongated morphology, would produce the opposite effect and result in substantially higher FIPs.

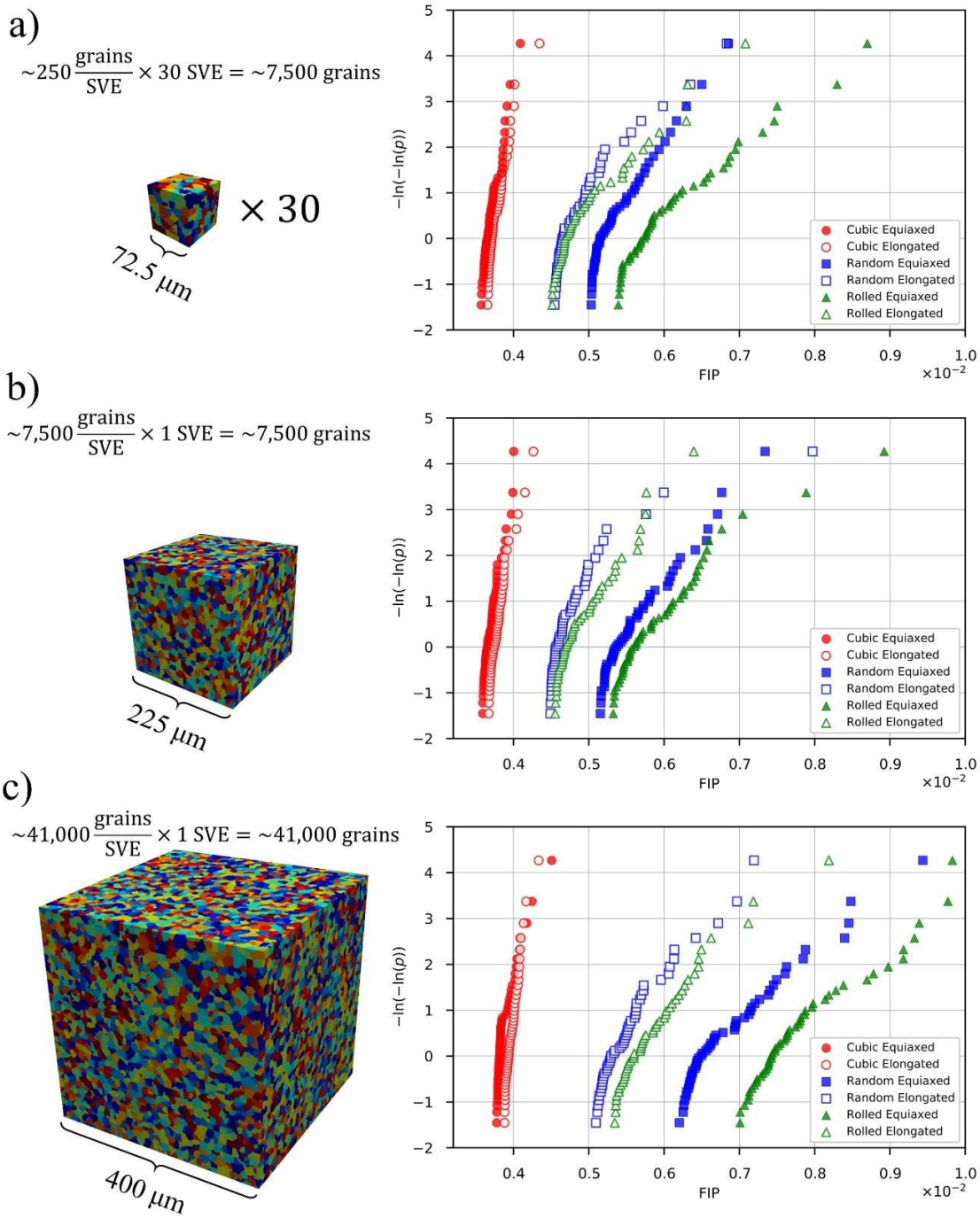

Fig. 3. Comparison of the highest 50 sub-band volume averaged FIPs from ensembles of SVEs with different grain morphologies and crystallographic textures. As larger SVEs are simulated, a greater number of critical grain orientations and neighborhood interactions that manifest high FIPs are captured. In a), ensembles of 30 smaller SVEs are simulated. The same total number of grains are simulated for each combination of crystallographic texture and grain morphology in b) but with a single

larger SVE. In c), an even larger SVE is simulated for each of the six data sets with more than five times as many grains.

3.2. Simulating larger volumes

As larger SVEs with more grains are simulated for a given target microstructure, the likelihood of capturing grains oriented favorably for significant slip increases. It will be shown later that grain orientation alone does not account for the highest FIPs, but it is nonetheless an important factor. FIPs from progressively larger SVEs are compared in Fig. 3b and Fig. 3c. The cubic textured FIPs show a minuscule increase, whereas the other textures and morphologies increase significantly. In particular, the equiaxed grain morphology for the random and rolled textures shows the largest increase in FIPs. Even though more than five times as many grains are simulated, the relatively smaller increase in cubic-textured FIPs is due to a reduced probability of grains oriented for significant slip. Analysis of the cubic ODF pole figure in Fig. 1c shows that on average, eight of the 12 available slip systems are equally activated with an apparent Schmid Factor (SF) of 0.41 [69]. On the other hand, grains favorably oriented for significant slip are much more likely in the other two textures. Using lines of best fit to the FIPs in Fig. 3b and Fig. 3c, we can compute the percent increase in the 99th percentile FIPs between the ~7,500 grain and ~41,000 grain SVEs. These are between 1.5% and 8.0% for the cubic texture and as high as 26.6% and 25.0% for the random and rolled textures, respectively (data available in Table S1 of the supplementary information). Therefore, it may be concluded that cubic-textured microstructure SVEs require on the order of tens of thousands of grains for FIP EVDs to begin to approach conditions of convergence to RVE size for this response.

4. FIP convergence and variability with SVE size

The results presented in Fig. 3 demonstrate that FIP convergence is primarily affected by the number of grains simulated. Here, four different SVE sizes are generated with random crystallographic texture and equiaxed grain morphology to examine the following scenarios:

- Whether the FIP EVDs from some number of SVEs comprising an ensemble converge to that of a single massive SVE comprising all the grains in the associated SVE ensemble
- Whether FIP EVDs tend to converge to some upper bound value as very large SVEs are simulated.

Each set contains progressively larger SVEs. A sample SVE from each of the four sets is shown in Fig. 4. The largest SVE contains over 160,000 grains discretized by a 2503 = 15,625,000 finite element (FE) mesh. The SVEs generated and simulated here demonstrate the powerful capabilities of the PRISMS-Fatigue framework not only in terms of scalability for massive SVE CPFEM simulations but also for pre- and post-processing of the associated data sets. Moreover, other material systems with a larger grain size can be generated with the same number of grains as the largest sample shown here but with a physical size approaching an actual laboratory specimen. For instance, at the same grain mesh resolution (~98 elements per grain), a material with a lognormal mean grain size of 60 µm yields a microstructural volume (RVE) with a side length of 2.625 mm. Crystal plasticity simulations previously inaccessible in more conventional serial FE codes are made possible using the high performance capability of PRISMS-Fatigue [41].

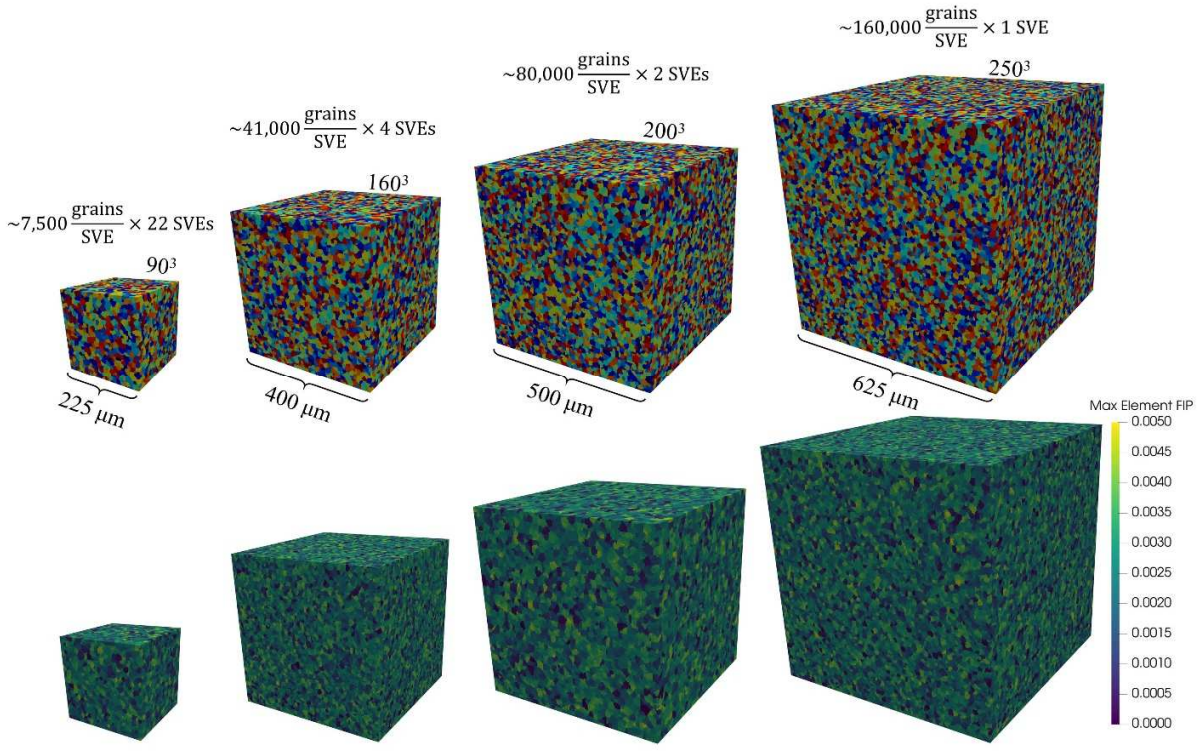

Fig. 4. SVEs with random crystallographic texture generated using DREAM.3D for the large scale FIP comparison. Each of the four SVE sets contain ~160,000 – 165,000 grains. The bottom row shows variation in element-level Fatigue Indicator Parameters (FIPs) throughout the samples. Although some element-level FIPs are larger than the legend maximum of 0.005, the purpose is to emphasize the heterogeneity of FIPs throughout the samples.

The overall cyclic stress-strain responses of the different sized SVEs in Fig. 4 were previously shown to be expectedly indistinguishable (see Fig. 3e in [41]). Each SVE set undergoes fully reversed uniaxial cyclic straining at a strain amplitude of 0.7%. The highest 100 FIPs are then extracted from each case individually and fit to the Gumbel EVD in Fig. 5a, Fig. 5b, and Fig. 5c for the ~7 500, ~41 000, and ~80 000 grain SVE sets, respectively. In Fig. 5d, the highest 100 FIPs from the entire ensemble of the three previous SVEs are compiled and fit to the Gumbel EVD alongside the 100 highest FIPs from the ~160,000 grain SVE. The variability between FIP EVDs is greatest across the 22 smallest ~7,500 grain SVEs. However, it is inappropriate to draw conclusions regarding FIP EVD variability between these figures since Fig. 5b and Fig. 5c depict only four and two data sets, respectively. It may be concluded, however, that more variability would be expected between the distributions in Fig. 5a since these SVEs contain the least number of grains. Thus, some SVEs will contain one or multiple grains that manifest higher FIPs compared to the others. Larger SVEs have increased probability of manifesting high FIPs because more grains are sampled [70]. Fig. 5c is striking because the two FIP EVDs appear almost indistinguishable. Two experimental specimen sets with different critically stressed volumes under identical applied stress or strain conditions would be expected to display different variability in fatigue response (e.g., fatigue life measured by number of cycles to form a crack on the order of grain size). The specimen set with the smaller critically stressed volume would unquestionably exhibit higher fatigue life due to a decreased probability of finding a critical hot spot for fatigue crack formation [70]. Moreover, it would also be expected to display higher variability in fatigue life because a relatively limited number of grains are sampled. It is important to note that FIP EVD variability is greatest in the low probability regime (i.e., high cumulative probability), particularly evident in Fig. 5a and Fig. 5b.

In Fig. 5d, the 100 highest FIPs from each of the previous three SVE sets are fit to the Gumbel EVD alongside the highest 100 FIPs from the ~160,000 grain SVE. There is remarkable overlap between all four data sets in the high probability regime towards the left in Fig. 5d, suggesting that any of the four microstructure sets can be individually pursued to generate a reliable FIP EVD, i.e., each set collectively establishes a reliable RVE for fatigue related applications. Furthermore, an ensemble of smaller SVEs or a single large SVE can both be used for relative fatigue rank ordering of microstructures based on FIP EVDs. There is, however, a distinct discrepancy in the low probability regime associated with the highest FIPs for each SVE or SVE ensemble. The eight highest FIPs from the ~160,000 grain SVE (purple star markers) deviate from the other three data sets. The grains that manifest these highest FIPs are investigated next. To the best of the authors' knowledge, the analysis of extreme value FIPs in the ~160,000 grain SVE here utilizes the largest microstructure-sensitive cyclic CPFEM simulation reported

to date [41], not considering other simulation schemes such as FFT crystal plasticity [28, 71], for example.

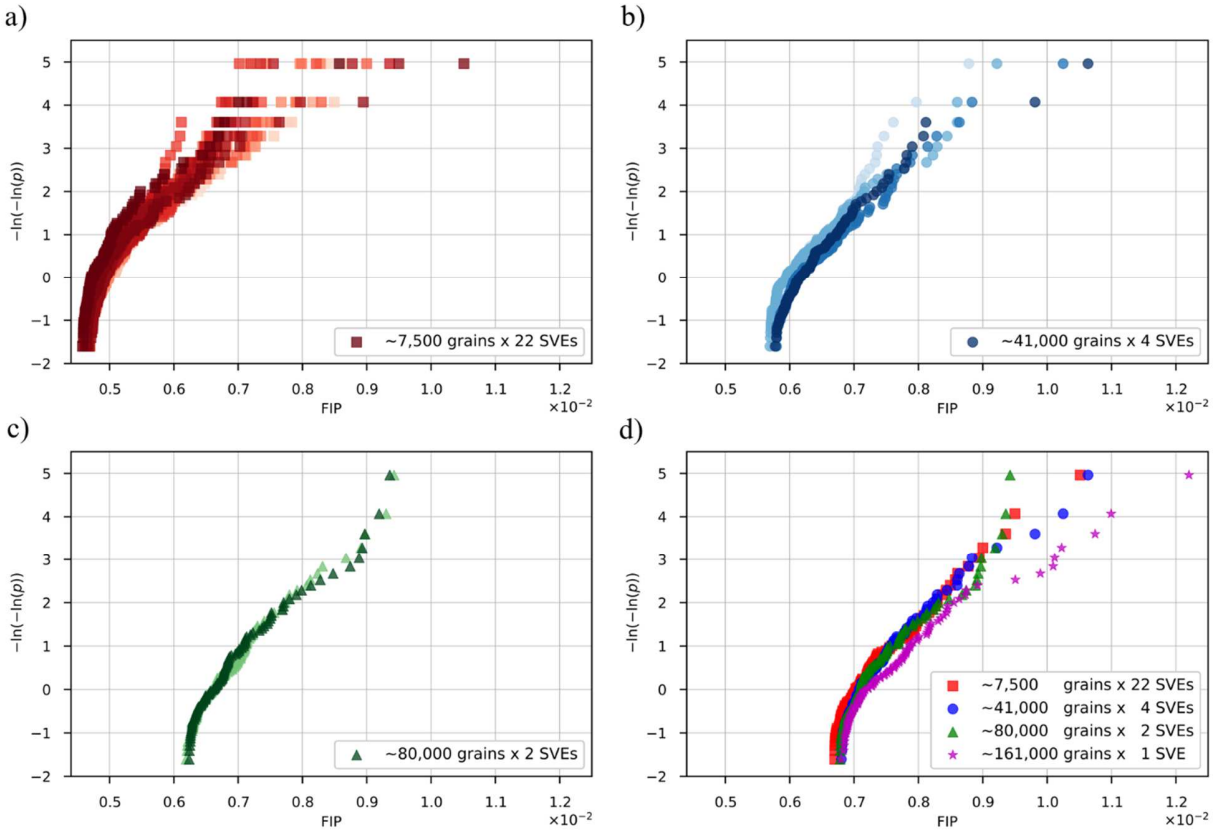

Fig. 5. The highest 100 FIPs compiled and fit to the Gumbel extreme value distribution for the SVE sets shown in Fig. 4: a) ~7,500 grains x 22 SVEs, b) ~41,000 grains x 4 SVEs, and c) ~80,000 grains x 2 SVEs. In d), the highest 100 FIPs from each of the previous SVE ensembles are compiled and plotted alongside the 100 highest FIPs from the ~160,000 grain SVE.

4.1. Material structure correlations for the hot spot grains

To exploit the massive scale of the ~160,000 grain SVE simulation, structural features in the neighborhoods of the distinctly high FIPs observed in Fig. 5d are further investigated here. The SF and equivalent grain diameters of the grains that manifest the highest FIPs are analyzed. Afterwards, more complex formulations for structural correlations are examined, including different neighborhood effects.

The apparent SFs of the slip systems that manifest the highest 50 sub-band volume averaged FIPs in the ~160,000 grain SVE are shown in Fig. 6a, where the color bar represents the sub-band volume averaged FIP. As expected, all 50 SFs are close to the maximum value of 0.5 but there is no correlation to

the highest ~5-10 FIPs, i.e., the SF alone does not explain why these certain grains manifest the highest FIPs. This accords with experimental observations: although cracks initiate mainly in grains with a rather high SF, other grains with similar characteristics do not develop damage [72]. Harte et al. [39] similarly demonstrated that grains with a high SF do not necessarily undergo large strain or deformation. As a note, the apparent SF is based solely on geometry and orientation of applied load. In contrast, the local SF considers the ratio of the maximum resolved shear stress divided by the global applied stress averaged over some volume and reflects the local stress state affected by intergranular interactions and microplasticity [73]. While the apparent SF is bounded by 0.5, the local SF can vary broadly between 0 and 1 due to load shielding or load shedding from neighboring grains [73].

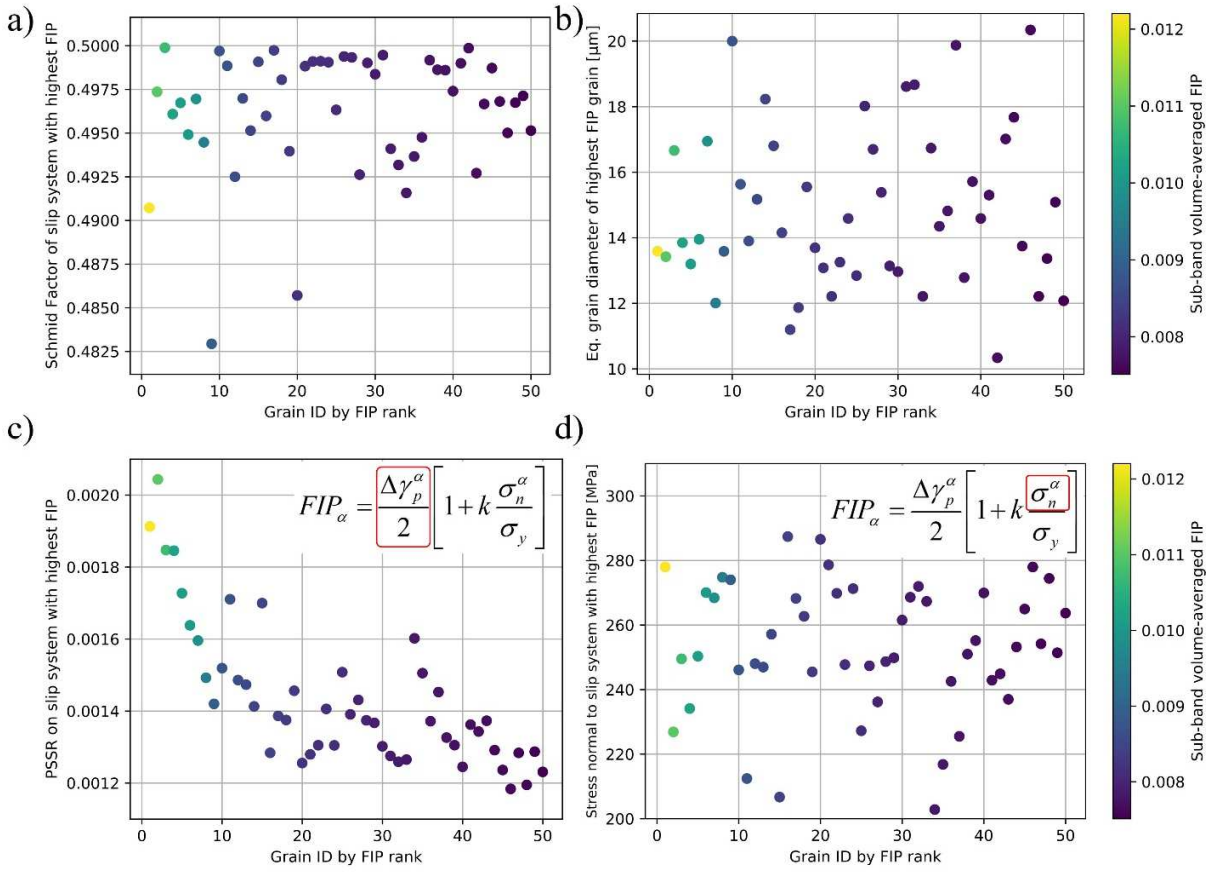

Fig. 6. Correlations of the highest 50 sub-band volume averaged FIPs from the ~160,000 grain SVE. a) shows the apparent Schmid Factor (SF) of the slip system with the highest FIP and b) shows the equivalent grain diameter as reported by DREAM.3D for the grains with the highest FIPs. In c) and d), the plastic shear strain range on the slip system with the highest FIP and the stress normal to the slip plane of the highest FIP, respectively, are shown. These are averaged over the same sub-band elements that manifest the highest FIPs. The color bar represents the sub-band volume averaged FIP value.

Although the CPFEM model employed here does not consider grain size effects, the increased mean free slip path in larger grains could result in an increased plastic shear strain range (PSSR) to manifest high FIPs [16, 74]. However, the equivalent grain diameters of the grains that manifest the highest 50 FIPs are portrayed in Fig. 6b and show that the highest FIPs are unrelated to grain size. Fig. 6c and Fig. 6d show the two components of the highest 50 sub-band volume averaged FIPs: the PSSR on the slip system and the peak stress normal to the slip plane, respectively. There is a strong correlation between the PSSR and the highest FIPs. However, the variation of FIPs and peak stress normal to slip planes exhibits no clear correlation.

Other attempts to correlate the highest ~5-10 FIPs to structural characteristics (e.g., misorientation between hot spot grains and their NNs, ratio of highest SF in hot spot grains to the SFs in NN grains, incorporating 1st or 1st and 2nd NN grains, etc.) are detailed in Section 3 of the supplementary information. However, these also provide no clear correlation to the highest FIPs in the ~160,000 grain SVE. The nuance in these correlation attempts is that the spatial position of grains is not considered, i.e., whether the hard and soft grains are located along the loading direction or transverse to the loading direction, as described in the introduction. Thus, relatively simple structural correlations inadvertently smear the effects of individual first and second NN grains. Clearly, more complex and higher-order statistics are required to investigate the structural features that manifest the high FIPs shown in Fig. 5d, such as those suggested by Kawano et al. [36, 37]. However, the much stronger and long-range grain-grain interactions characteristic of higher symmetry FCC alloys may still prove problematic [17, 39], especially using the two-term back stress formulation employed in this work. Although these results demonstrate that simple structural correlations are insufficient to determine hot spot grains, we can quantify the influence of NN grains on hot spot grains by varying certain NN grain orientations.

5. Quantifying nearest neighbor influence

The previous section demonstrated that correlations between microstructure and hot spot grains are nontrivial. As an alternative, the influence of NN grains on the response of hot spot grains is systematically investigated in this section.

5.1. Cropped microstructure SVEs

The grains that manifest the three highest sub-band volume averaged FIPs in the ~160,000 grain SVE are shown in Fig. 7. The goal of this section is to examine the extreme value response in these grains as the orientations of NN grains are altered. Therefore, we must first extract a suitably large neighborhood centered about these grains and then simulate these smaller SVEs at the same cyclic strain conditions as before. A SVE with ~4,600 grains discretized by 723 finite elements is selected and extracted, centered about the grains that manifest the first and third highest sub-band volume averaged FIPs in the ~160,000 grain SVE (shown as two green cubes in Fig. 7). The grain that manifests the second highest FIP is not considered in this section because it is much closer to the boundary of the ~160,000 grain SVE (shown as the red rectangular prism in Fig. 7), and a smaller SVE as described above with this grain at the center cannot be extracted. The two cubic cropped regions with ~4,600 grains in Fig. 7 are subjected to the same cyclic strain conditions as the previous SVEs, i.e., fully reversed uniaxial cyclic straining at 0.7% strain amplitude. Periodic boundary conditions are prescribed to retain bulk, subsurface material response. The first and third highest sub-band volume averaged FIPs have values of 1.22 x 10-2 and 1.07 x 10-2, respectively, in the ~160,000 grain SVE. After the two ~4,600 grain SVEs are cropped and subjected to cyclic straining, the highest FIPs still occur in the same grain about which the SVEs are centered (and over the same slip bands), and the values change only slightly to 1.20 x 10-2 and 1.10 x 10-2, respectively. It is thus evident that altering the SVE neighborhood very far from the grains of interest has a small but negligible effect on the computed FIPs. In the subsequent analysis, the responses of the ~4,600 grain SVEs are considered as the baseline for comparison.

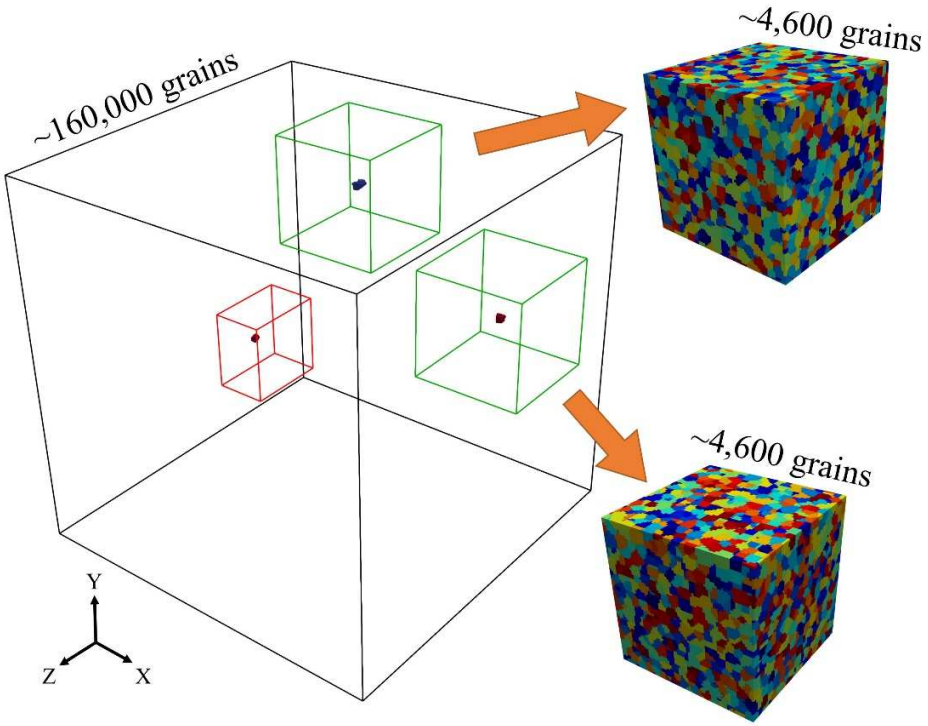

Fig. 7. Location of the three highest FIPs in the ~160,000 grain SVE discretized by 2503 voxels. New SVEs with ~4,600 grains discretized by a 723 FE mesh are cropped about the grains that manifest the first and third highest FIPs (shown as cubes with green edges). These SVEs are then subjected to the same cyclic straining conditions as the ~160,000 grain SVE (i.e., fully reversed uniaxial cyclic straining to 0.7% strain) to quantify the influence of nearest neighbor grains on the FIP response in the center grain of interest. The second highest FIP grain is not considered because it is too close to the SVE boundary (shown as the rectangular prism with red edges).

To quantify the influence of NN grains on the response of the grain of interest (GOI) about which the cropped regions are centered, the grain orientations of certain NN grains are systematically changed. The NN grains are first assigned to different layers as demonstrated in Fig. 8. The GOI that manifested the highest FIP in the ~160,000 grain SVE and about which the first ~4,600 grain SVE is centered is shown in Fig. 8a. Fig. 8b shows a clipped half-view of the first NN grains. The remaining subplots in this figure display clipped views of the second, third, fourth, and fifth NN grain layers.

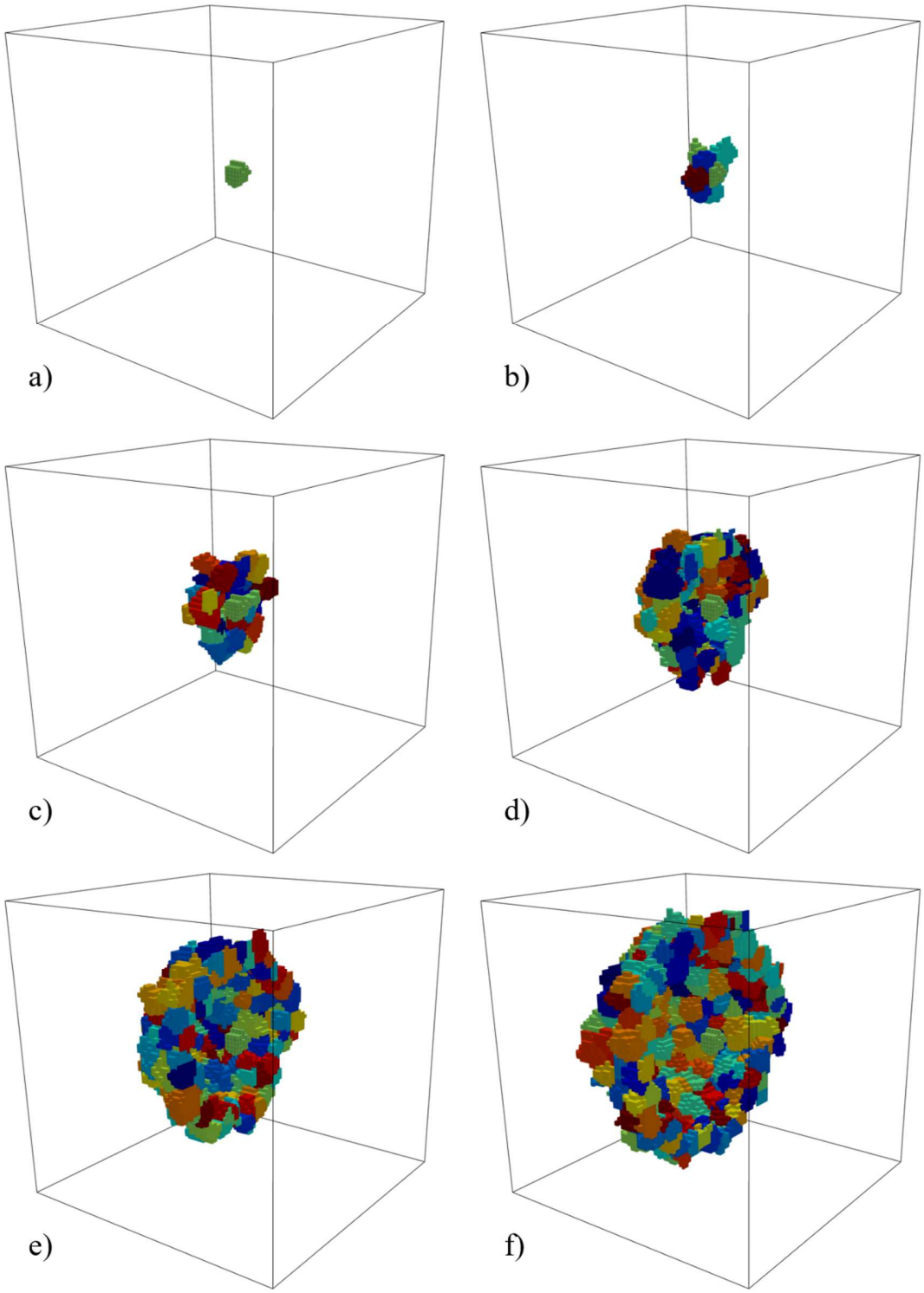

Fig. 8. a) The grain with the highest FIP in the original ~160,000 grain SVE cropped to a smaller domain with ~4,600 grains discretized by a 723 FE mesh. Layers with the first, second, third, fourth, and fifth nearest neighbors are shown in b), c), d), e), and f), respectively. Nearest neighbor grains are defined as those that share at least one element face.

Grain orientations are systematically changed, and several scenarios are investigated. In the first scenario, the grain orientation of the single largest grain in one of the NN grain layers is altered. This is repeated for all five NN grain layers. In the next scenario, all orientations in a NN grain layer are altered and this is once again repeated for all five layers. Finally, for the first NN grain layer, the orientation of the grain that shares the most surface area with the GOI is also altered. Although this is not the largest grain in the first NN grain layer, it may have a more pronounced effect on the response of the GOI. Additional scenarios are investigated for the 3rd, 4th, and 5th NN grain layers (see Section 4 of the supplementary information). These include altering the grain orientations of the five largest grains, the 5% largest grains, and the 20% largest grains. Table 2 contains statistics for the five NN grain layers in the ~4,600 grain SVEs.

Table 2. Nearest neighbor grain layer statistics for the first and second ~4,600 grain SVEs cropped about the 1st and 3rd highest FIP, respectively.

	First ~4,600 grain SVE		Second ~4,600 grain SVE	
Layer Number	Number of total grains	Number of elements in largest grain	Number of total grains	Number of elements in largest grain
1	13	209	20	251
2	68	226	68	222
3	159	319	173	287
4	303	291	353	285
5	517	305	597	285

For each scenario describe above, new grain orientations are randomly selected five times to capture variability in NN grain effects. In the case where a single orientation is altered in the first NN grain layer, the sampling is performed ten times. The altered SVEs then undergo the same FIP calculation and volume averaging as before. For both cropped SVEs, two additional 1st NN grain modifications include setting the grain orientations of the largest grain and the grain that shares the most surface area with the GOI to the orientation of the GOI. In addition to the FIP defined in Eq. (9), the maximum sub-band volume averaged PSSR calculated across the final straining cycle and the peak stress normal to a slip plane (σ_n) are also considered.

5.2. Cropped region about the 1st highest FIP

Fig. 9a and Fig. 9b show the highest sub-band volume averaged PSSR and FIP, respectively, for the first ~4,600 grain SVE. This figure depicts the response variables in the GOI after one or multiple NN grain orientations are changed. The first two columns in Fig. 9a and Fig. 9b contain data from 10 simulations, whereas the following nine columns each contain data from five simulations. The last two data points are each extracted from a single simulation and thus, the data in Fig. 9 is extracted from a total of 67 simulations. In a few cases, the highest PSSR or FIP no longer occurs within the GOI. For instance, when the orientations of all 13 NN grains in the 1st layer or all 68 NN grains in the 2nd layer are altered (7th and 8th data sets in Fig. 9), the red triangle markers indicate that the highest response variables now occur elsewhere in another grain. The PSSRs and FIPs in Fig. 9 shows similar trends and different magnitudes. The maximum value of σ_n in the entire first ~4,600 grain SVE ranged between 535.5 MPa and 539.0 MPa for all 67 simulations. Further investigation revealed small variations to σ_n in the GOI. The maximum values of σ_n in the GOI for all 67 simulations ranged between 346.5 MPa and 370.9 MPa, which were the extremes and occurred in the case where all 2nd NN grain orientations and all 1st NN grain orientations were altered, respectively. σ_n in the GOI was 358.1 MPa with no altered grain orientations.

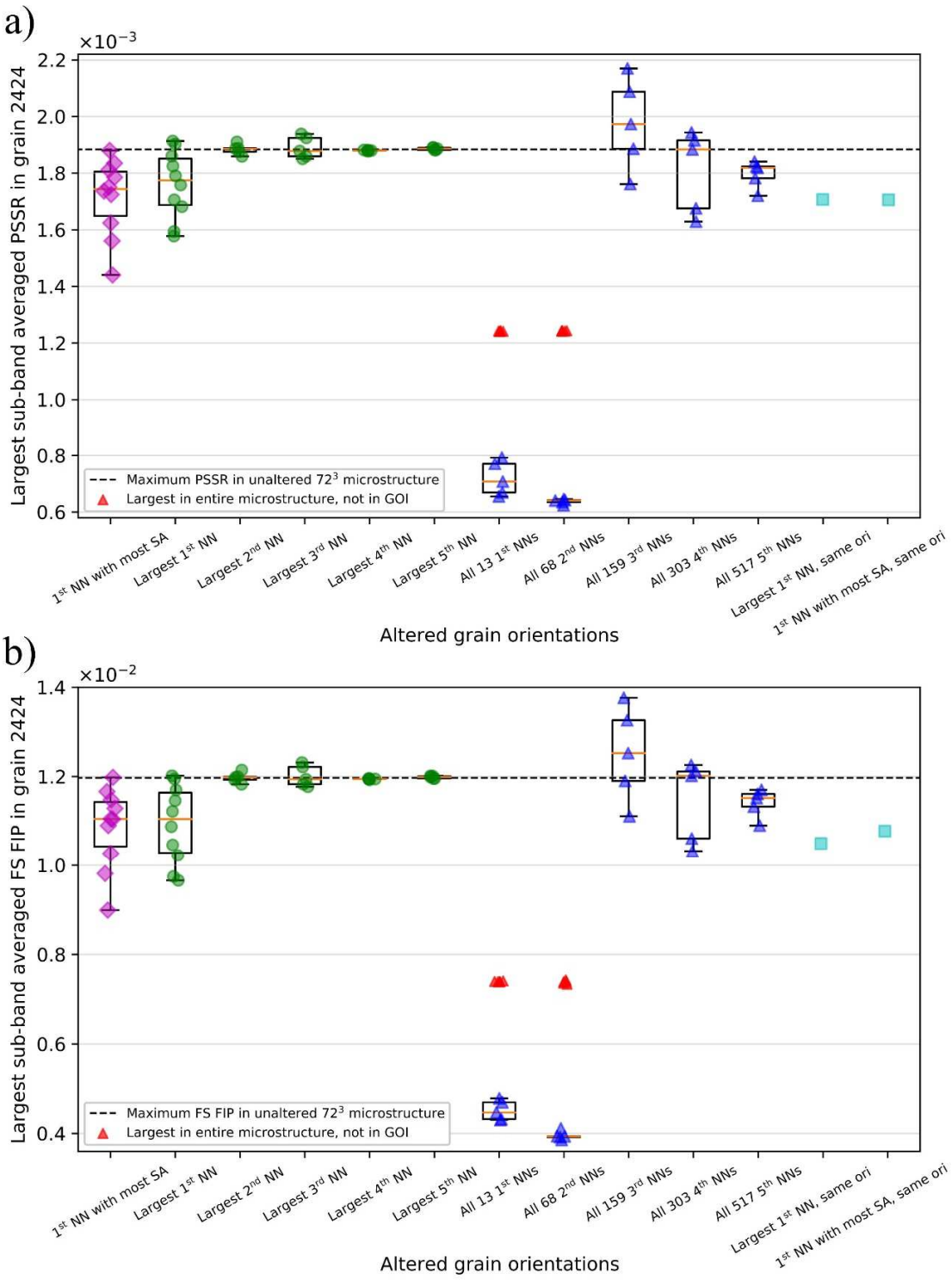

Fig. 9. The highest sub-band volume averaged a) PSSR and b) FIP in the grain (#2424) about which the first ~4,600 grain SVE was cropped from the ~160,000 grain SVE as a function of changes to grain nearest neighbor orientation(s). The black dashed line indicates the highest PSSR or FIP in this grain without changing NN grain orientations. Red triangle markers indicate the highest PSSR or FIP that did not occur within grain #2424.

The first data sets in Fig. 9a and Fig. 9b (magenta diamond markers) show response variability in the GOI after the orientation of the 1st NN grain that shares the most surface area with the GOI is altered. The lowest PSSR and FIP is reduced by 23.5% and 24.9%, respectively, as compared to the unaltered SVE. This emphasizes the influence of 1st NN grain interactions, where a change in orientation can reduce the extreme value response in a hot spot grain by nearly 25%.

The next five data sets (green circle markers) show the response variability after the orientation of the single largest NN grain in each of the five layers is altered. This effect is most significant for the 1st NN grain layer and quickly decays. Surprisingly, the maximum response variable is in some cases larger than in the unaltered SVE simulation. Changes to the orientation of the largest NN grain in the 4th and 5th layers does not influence the GOI. The subsequent five data sets (blue triangle markers) show the response variability after all grain orientations in each of the five layers are altered. A change to all grain orientations in the first two layers sufficiently perturbs the micromechanical response to drive the highest response variable to a different grain, as indicated by the red triangle markers. When all 3rd NN grain orientations are altered, however, the highest PSSR or FIP returns to the GOI, and in three out of the five cases the response is now larger than the response of the unaltered SVEs. Finally, the two cyan square markers in Fig. 9a and Fig. 9b depict the response when the orientations of the largest 1st NN grain and the 1st NN grain that shares the most surface area (SA) with the GOI are equal the orientation of the GOI. The response is reduced in both cases and these two scenarios are investigated in more detail later.

The PSSR and σ_n both contribute to the FIP of interest in this work. The similarities between Fig. 9a and Fig. 9b suggest that σ_n is not significantly affected by changes to orientations of NN grains. The coefficient of variation (COV, defined as the standard deviation of a data set divided by the mean) for the response variables in Fig. 9 and σ_n is shown in Fig. 10 and emphasizes that σ_n is weakly perturbed by changes to orientations of NN grains.

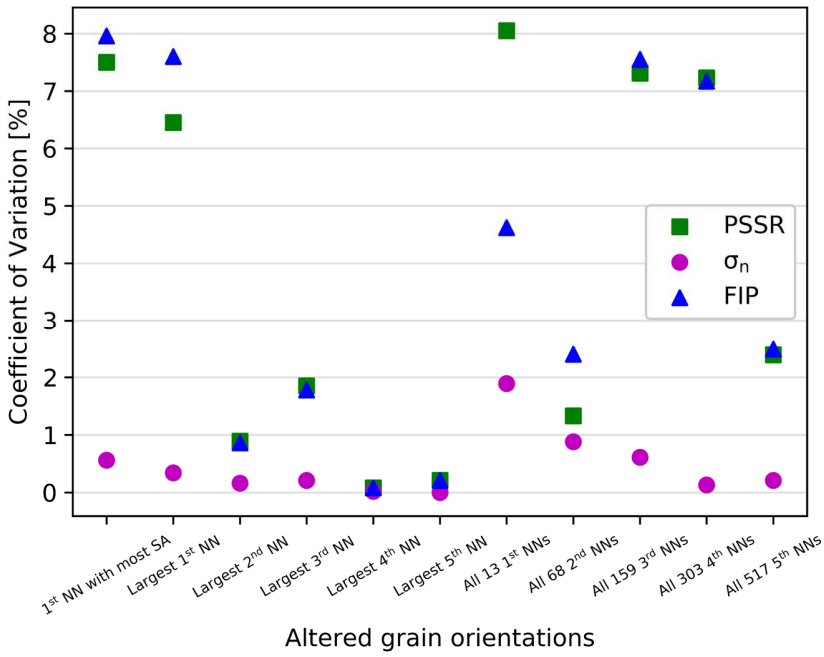

Fig. 10. Coefficient of Variation for the response variables of the first ~4,600 grain cropped SVE, using data shown in Fig. 9.

5.3. Cropped region about the 3rd highest FIP

The analysis in the previous section is repeated for the second ~4,600 grain cropped SVE. Only the response variability of the maximum sub-band volume averaged FIP is shown due to the similarities between the FIP and PSSR observed in Fig. 9. Fig. 11 shows similar trends to the data presented in Fig. 9. For instance, altering the largest NN grain in each layer only perturbs the GOI up to the third layer. Similarly, the effect of altering all NN grains in progressively distanced layers appears to decay, but not as quickly as altering the single largest NN grain in each layer, because in the former scenario, several hundreds of grain orientations are altered. There are interesting contrasts in this second ~4,600 SVE. First, there is greater response variability when the largest 1st NN grain orientation is altered versus the 1st NN that shares the most surface area with the GOI. Furthermore, the two cyan square markers indicate that changing the orientation of these two 1st NN grains to the same orientation as the GOI has little influence on the GOI. These trends are explored further.

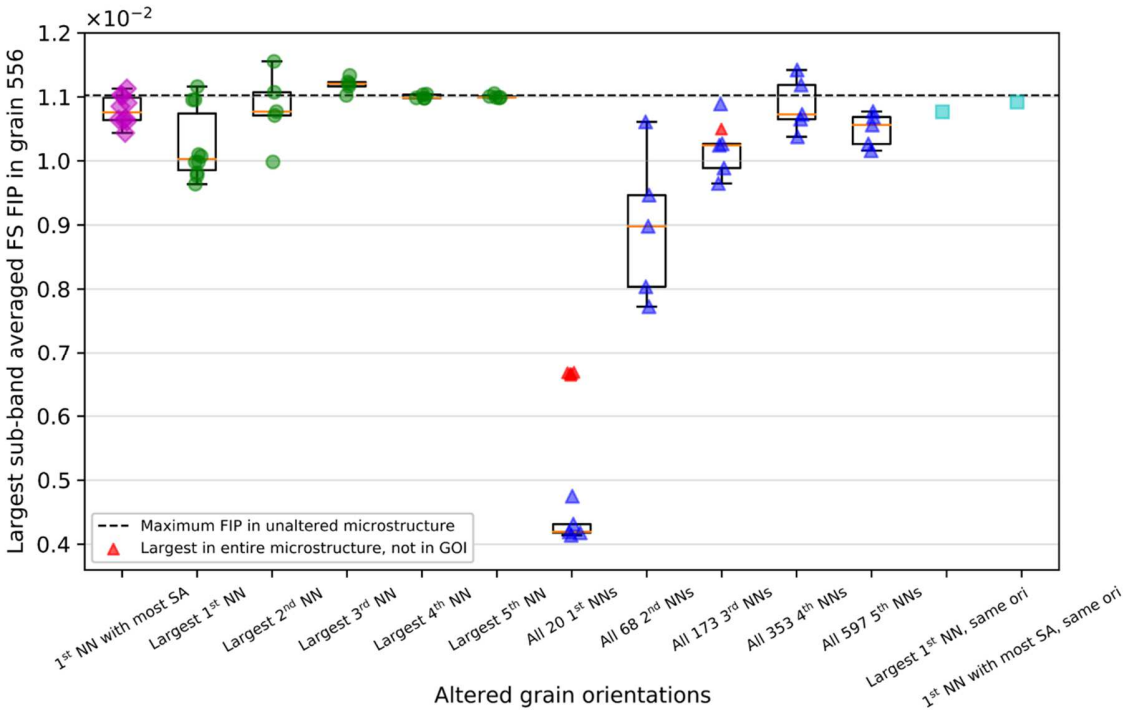

Fig. 11. The highest sub-band volume averaged FIP in the grain (#556) about which the second ~4,600 grain SVE was cropped from the ~160,000 grain SVE as a function of changes to grain nearest neighbor orientation(s). The black dashed line indicates the highest FIP in this grain without changing NN grain orientations. Red triangle markers indicate the highest FIP that did not occur within grain #556.

5.4. Discussion of nearest neighbor influence

To further investigate the response variability in the GOI when a single grain orientation in the first NN layer is altered, Fig. 12 depicts the grains that manifest the 1st and 3rd highest FIPs (about which the two ~4,600 grain SVE were cropped), along with the grains whose orientations were altered to produce the first two and last two data sets in Fig. 9 and Fig. 11, respectively. Table 3 contains the apparent SFs of each grain.

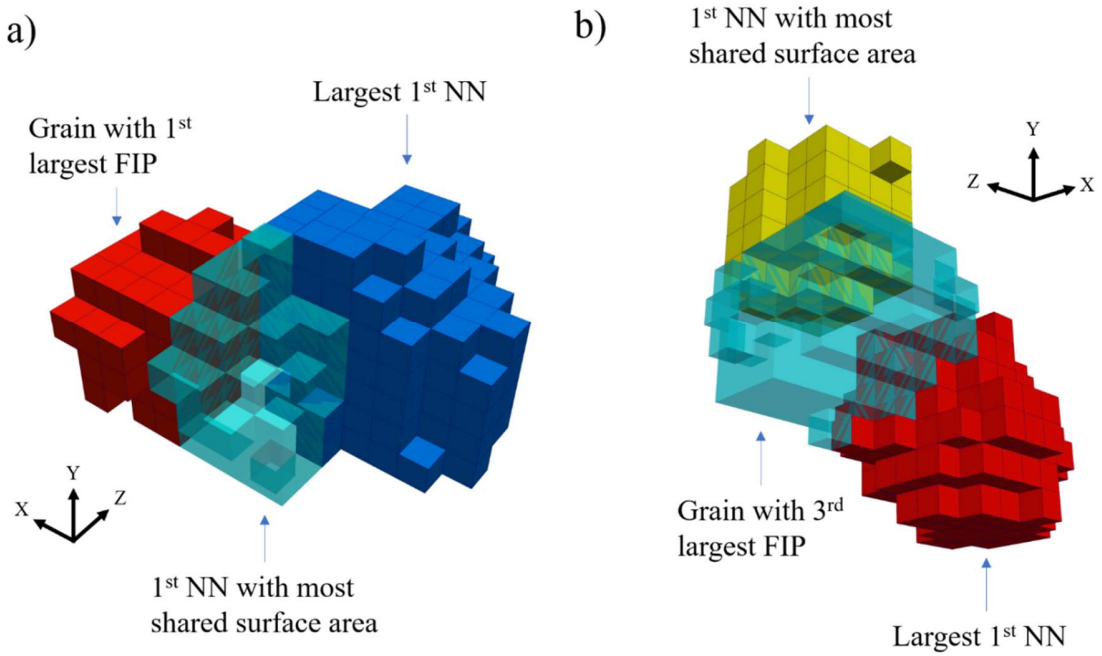

Fig. 12. The grains that manifest the a) 1st (grain #2424) and b) 3rd (grain #556) highest FIPs in the ~160,000 grain SVE. The 1st NN grains that share the most surface area with the grains of interest and the largest 1st NN grains are shown. SVEs were strained uniaxially in the X direction. Some grains are shown as opaque to improve visualization.

Table 3. Apparent Schmid Factors (SF) of the six grains depicted in Fig. 12.

Slip planes	(1,1,1)			(-1,1,1)			(1,1,-1)			(1,-1,1)		
Slip directions	[0,1,-1]	[-1,0,1]	[1,-1,0]	[0,-1,1]	[-1,0,-1]	[1,1,0]	[0,-1,-1]	[1,0,1]	[-1,1,0]	[0,1,1]	[1,0,-1]	[-1,-1,0]
1st highest FIP grain												
Grain of interest (#2424)	0.32	0.49	0.17	0.10	0.13	0.23	0.26	0.45	0.20	0.04	0.09	0.14
Largest 1st NN	0.07	0.23	0.30	0.20	0.09	0.11	0.12	0.01	0.13	0.40	0.34	0.06
Most shared area	0.06	0.20	0.26	0.20	0.13	0.06	0.14	0.02	0.16	0.40	0.36	0.03
3rd highest FIP grain												
Grain of interest (#556)	0.50	0.24	0.26	0.17	0.05	0.23	0.47	0.17	0.30	0.20	0.12	0.33
Largest 1st NN	0.35	0.44	0.09	0.43	0.43	0.00	0.44	0.36	0.09	0.35	0.35	0.00

Most shared area	0.00	0.24	0.24	0.00	0.41	0.41	0.17	0.13	0.05	0.17	0.05	0.13

SVEs were strained in the X direction and Fig. 12 reveals that the position of these 1st NN grains may explain the difference in response variability observed in Fig. 9 and Fig. 11. The 1st NN grain that shares the most surface area with grain #2424 (Fig. 12a) is positioned directly along the straining direction and the largest 1st NN grain is offset in the straining and Z directions. In contrast, the two 1st NN grains of grain #556 (Fig. 12b) are offset in the Y and Z directions with roughly the same center of mass in the X direction. This suggests that the extreme value fatigue response of hot spot grains is more sensitive to changes in the orientations of NN grains along the SVE straining direction, since the first two data sets in Fig. 9a and Fig. 9b vary much more significantly than the first two data sets in Fig. 11.

Setting the orientations of the two 1st NN grains in Fig. 12 to the orientations of grain #2424 and grain #556 perturbs the response of the GOI differently, and these effects are difficult to predict. The last two data sets in Fig. 9a and Fig. 9b showed a substantial decrease in response variables, whereas the last two data sets in Fig. 11 showed nearly negligible change. Both grain #2424 and grain #556 have maximum SFs of 0.49 and 0.50, respectively, as shown in Table 3. Table 3 shows that the maximum apparent SFs for the two grains that share the most surface area with the GOIs are similar and close to 0.40-0.41. Altering these grain orientations raises the maximum SFs to ~0.49-0.50. The next important factor is the position of these 1st NN grains, which in one case is positioned directly along the straining direction and in the other, positioned along the Y direction of the GOI. In the latter case (Fig. 12b), the difference in GOI response is almost negligible, as indicated by the last data marker in Fig. 11. In contrast, the last data marker in Fig. 9b indicates that the position of the 1st NN grain that shares the most surface area with grain #2424 (Fig. 12a) strongly reduces the plastic deformation in grain #2424. This argument is complicated for the scenario in which the orientation of the largest 1st NN grain is changed to the orientation of the GOI because the change in maximum SF for the two largest 1st NN grains is different. Such spatial considerations are particularly important for low symmetry alloys in which hard-soft rogue grain combinations have been suggested to contribute to dwell fatigue failure [32-34], as described in the introduction. The analysis presented here emphasizes the need for advanced spatial correlations (e.g., convolutional neural networks [75], n-point statistics [76], or even the slip operation factor (SOF) by Kawano et al. [36, 37]). It may be the case, however, that the use of Schmid Factors will not yield useful results even with the advanced techniques mentioned above, since the

earlier section of this work and other works (e.g., [39, 40]) have demonstrated that the Schmid Factor is more applicable/useful in more anisotropic low crystallographic symmetry (e.g., HCP) material systems.

6. Discussion

This work examined the extreme value response of progressively larger SVEs with different crystallographic textures and grain morphologies to explore trends in FIP EVDs as a function of maximum SVE size; large single SVE FIP EVDs were compared to those of ensembles of SVEs comprising the same cumulative volume of microstructure. The trends of the FIP EVDs from different SVE sets, the largest of which contained over 160,000 grains discretized by a ~15.6 million finite element mesh, shows a progressive increase in the maximum computed extreme value FIPs. While RVE size has not been resolved with these simulations, the monotonicity of the increase of FIP EVDs with increase of SVE size and with number of smaller SVE ensembles, along with preservation of relative rank ordering of FIP EVDs for several microstructures, indicates that the process of convergence towards a RVE should be smooth and continuous, and that SVE ensembles indeed are useful for ranking microstructures in terms of relative resistance to fatigue crack formation. While convergence of the macroscopic stress-strain response has been previously shown to require only on the order of hundreds of grains, convergence of the FIP EVDs requires significantly more grains. The cubic crystallographic texture may require tens of thousands of grains for convergence of FIP EVDs. In contrast, the increased probability of individual grains oriented favorably for significant plastic slip in microstructures with random or rolled crystallographic textures requires substantially more grains for convergence of the FIP EVDs. Crystallographic texture is significantly more influential in this regard than grain morphology.

Four different SVE sets, each with over ~160,000 grains, demonstrated that an ensemble of smaller SVEs may be simulated to accumulate a near equivalent distribution of extreme value FIPs as compared to a single massive SVE. The eight distinctly high FIPs from the ~160,000 grain SVE were investigated to elucidate structural correlations of the hot spot grains. Nontrivial structural correlations at the most extreme fatigue hot spots revealed the need for more advanced formulations (e.g., convolutional neural networks [75], n-point statistics [76]) to better understand the connection between structure and extreme value response. Finally, a unique study in which individual grain orientations

were systematically altered investigated the variability at hot spot grains. Changes to a single grain orientation only affected the extreme value response of the hot spot grain up to the third layer of NN grains, in accordance with the work of Diehl et al. [31]. Further investigation suggested that the spatial location of the 1st NN grains with respect to the global straining direction may also influence response variability in the hot spot grains [38].

The effects of grain NN interactions are also expected to strongly depend on the material system and constitutive model employed. For instance, previous work demonstrated that the influence of a free surface in polycrystalline simulations of HCP Ti alloy Ti-6Al-4V decayed more rapidly as compared to the FCC Al 7075-T6 alloy explored in this work [17]. Furthermore, the two term Ohno-Wang type hardening law in this constitutive model, which was essential during model calibration to match experimentally measured plastic strain at low levels of applied stress, undoubtably influences the extent of NN grain interactions differently than other hardening models (e.g., Armstrong-Frederick hardening model). The simulation of massive microstructure SVEs enabled by the PRISMS-Fatigue framework is necessary to simulate sufficient grain/phase heterogeneity that leads to the extreme value responses investigated here. We emphasize that out of the ~160,000 simulated grains in the largest SVE, only eight manifested distinctly high FIPs. Thus, attempts to leverage data science and machine learning techniques in these problems will rely on the availability of massive data sets that PRISMS-Fatigue can provide.

7. Conclusions

In this work, large-scale CPFEM simulations are leveraged to determine the extreme value cumulative distributions of FIPs for progressively larger SVEs. The sensitivity of the EVD FIP response at hot spot grains is then investigated. The main findings can be summarized as:

- An ensemble of smaller SVEs or a single, equivalently large SVE can be used to rank order the fatigue resistance of polycrystalline materials with different crystallographic textures and grain morphologies.
- Although the cubic crystallographic texture achieves nearly converged EV FIP response with ~41,000 grains (i.e., the FIP EVDs appear to converge between ~7,500 and ~41,000 grain microstructure SVEs), the random and rolled textured FIP EVDs do not converge. However, data

from these other crystallographic textures may still be used for purposes of rank ordering fatigue resistance of microstructures (e.g., textures).

- An ensemble of relatively smaller SVEs (e.g., 22 SVEs each with ~7,500 grains) can be used to build equivalent FIP EVD statistics to that of a single very large SVE (e.g., a single SVE with ~160,000 grains) in the high to medium probability regime. However, deviations in the low probability regime indicate that the highest FIPs do not yet converge. Future work might determine whether even larger SVEs/more grains must be simulated to reach a FIP upper limit, and to determine the complex structural correlations that associate with these high FIPs.
- Simple microstructure parameters (e.g., Schmid Factor, grain size, nearest neighbor misorientation, use of 1st and 2nd nearest neighbor grains, etc.) were unable to completely correlate to fatigue hot spot grains in the largest SVE simulated. These correlations depend not only on the microstructure but also on the crystal plasticity models employed (e.g., the two-term Ohno-Wang back stress formation with short- and long-range components). More advanced correlation techniques may be required to elucidate these relationships (e.g., convolutional neural networks [75], n-point statistics [76]) which may rely on the availability of massive data sets that PRISMS-Fatigue can provide.
- The sensitivity of the extreme value FIP response at hot spot grains extends to the 3rd nearest neighbor when a single neighborhood grain orientation is altered. Changing the orientation of a hot spot grain's 1st nearest neighbor can reduce the maximum FIP in the microstructure by nearly 25%. Moreover, changing the orientation(s) of more distant nearest neighbor(s) (in the 2nd through 5th nearest neighbor layers) can substantially change the FIP in the hot spot grain.
- It is primarily the plastic shear strain range that is perturbed when the orientations of nearest neighbor grains are altered. In contrast, the stress component of the FIP used in this work (peak stress normal to the slip plane) exhibits a much lower coefficient of variation.
- The variability in the extreme value response at hot spot grains due to changes in orientations of nearest neighbor grains is complicated by the orientation, position, and size of the nearest neighbor grains. Attempts to understand these interactions without advanced data analysis frameworks may be untenable.

Acknowledgements

KSS and DLM are grateful for the support from the Office of Naval Research under grant number N00014-18-1-2784. MY and JEA are grateful for the support from the U.S. Department of Energy, Office of Basic Energy Sciences, Division of Materials Sciences and Engineering under Award #DE-SC0008637 as part of the Center for PRedictive Integrated Structural Materials Science (PRISMS Center) at University of Michigan. This work used the Extreme Science and Engineering Discovery Environment (XSEDE), which is supported by National Science Foundation grant number ACI-1548562, through the allocation TG-MSS160003. This research was supported in part through research cyberinfrastructure resources and services provided by the Partnership for an Advanced Computing Environment (PACE) at the Georgia Institute of Technology, Atlanta, Georgia, USA.

Data Availability

The DREAM.3D generated microstructures, CPFEM input files, PRISMS-Plasticity raw simulation results, and plots are available on Materials Commons at https://doi.org/10.13011/m3-31wm-h036. The Python scripts necessary to reproduce the results of this article are available at https://github.com/prisms-center/Fatigue.

Code Availability

PRISMS-Plasticity and PRISMS-Fatigue are open-source computer codes available for download at https://github.com/prisms-center/plasticity and https://github.com/prisms-center/Fatigue, respectively. In addition to written tutorials available in the GitHub repositories, a series of video tutorials totaling nearly two and three hours of content are available at https://www.youtube.com/playlist?list=PL4yBCojM4Swqy4FRteqxHWSiM1uiOOesj and https://www.youtube.com/playlist?list=PL4yBCojM4Swo3CvlA57syFrzk3p1mugP5, respectively.

References

[1] M. Yaghoobi et al., "Prisms-plasticity: An open-source crystal plasticity finite element software," Comput. Mater. Sci., 169, 109078 (2019)

[2] S. Kotha, D. Ozturk, and S. Ghosh, "Uncertainty-quantified parametrically homogenized constitutive models (uq-phcms) for dual-phase α/β titanium alloys," NPJ Comput. Mater., 6, 117 (2020)

[3] D. L. McDowell and F. P. E. Dunne, "Microstructure-sensitive computational modeling of fatigue crack formation," Int. J. Fatigue, 32, 1521 (2010)
[4] R. Hill, "Elastic properties of reinforced solids: Some theoretical principles," J. Mech. Phys. Solids, 11, 357 (1963)
[5] T. Kanit, S. Forest, I. Galliet, V. Mounoury, and D. Jeulin, "Determination of the size of the representative volume element for random composites: Statistical and numerical approach," Int. J. Solids Struct., 40, 3647 (2003)
[6] F. Qayyum, A. A. Chaudhry, S. Guk, M. Schmidtchen, R. Kawalla, and U. Prahl, "Effect of 3d representative volume element (rve) thickness on stress and strain partitioning in crystal plasticity simulations of multi-phase materials," Crystals, 10, 944 (2020)
[7] F. Qayyum, M. Umar, S. Guk, M. Schmidtchen, R. Kawalla, and U. Prahl, "Effect of the 3rd dimension within the representative volume element (rve) on damage initiation and propagation during full-phase numerical simulations of single and multi-phase steels," Materials, 14, 42 (2021)
[8] H. J. Bong, H. Lim, M.-G. Lee, D. T. Fullwood, E. R. Homer, and R. H. Wagoner, "An rve procedure for micromechanical prediction of mechanical behavior of dual-phase steel," Mater. Sci. Eng. A, 695, 101 (2017)
[9] M. Bouchedjra, T. Kanit, C. Boulemia, A. Amrouche, and M. E. A. Belouchrani, "Determination of the rve size for polycrystal metals to predict monotonic and cyclic elastoplastic behavior: Statistical and numerical approach with new criteria," Eur. J. Mech. A Solids, 72, 1 (2018)
[10] H. Lim, C. C. Battaile, J. E. Bishop, and J. W. Foulk, "Investigating mesh sensitivity and polycrystalline rves in crystal plasticity finite element simulations," Int. J. Plast., 121, 101 (2019)
[11] X. Tu, A. Shahba, J. Shen, and S. Ghosh, "Microstructure and property based statistically equivalent rves for polycrystalline-polyphase aluminum alloys," Int. J. Plast., 115, 268 (2019)
[12] M. D. Sangid, J. Rotella, D. Naragani, J.-S. Park, P. Kenesei, and P. A. Shade, "A complete grain-level assessment of the stress-strain evolution and associated deformation response in polycrystalline alloys," Acta Mater., 201, 36 (2020)
[13] T. Ozturk et al., "Simulation domain size requirements for elastic response of 3d polycrystalline materials," Modell. Simul. Mater. Sci. Eng., 24, 015006 (2015)
[14] S. Bargmann et al., "Generation of 3d representative volume elements for heterogeneous materials: A review," Prog. Mater Sci., 96, 322 (2018)
[15] D. L. McDowell, "Simulation-based strategies for microstructure-sensitive fatigue modeling," Mater. Sci. Eng. A, 468-470, 4 (2007)
[16] G. M. Castelluccio and D. L. McDowell, "Mesoscale modeling of microstructurally small fatigue cracks in metallic polycrystals," Mater. Sci. Eng. A, 598, 34 (2014)
[17] K. S. Stopka and D. L. McDowell, "Microstructure-sensitive computational estimates of driving forces for surface versus subsurface fatigue crack formation in duplex ti-6al-4v and al 7075-t6," JOM, 72, 28 (2020)
[18] H. Hallberg, S. K. Ås, and B. Skallerud, "Crystal plasticity modeling of microstructure influence on fatigue crack initiation in extruded al6082-t6 with surface irregularities," Int. J. Fatigue, 111, 16 (2018)
[19] A. Le Pécheur, F. Curtit, M. Clavel, J. M. Stephan, C. Rey, and P. Bompard, "Polycrystal modelling of fatigue: Pre-hardening and surface roughness effects on damage initiation for 304l stainless steel," Int. J. Fatigue, 45, 48 (2012)
[20] R. Bandyopadhyay and M. D. Sangid, "Crystal plasticity assessment of inclusion- and matrix-driven competing failure modes in a nickel-base superalloy," Acta Mater., 177, 20 (2019)

[21] V. Prithivirajan and M. D. Sangid, "Examining metrics for fatigue life predictions of additively manufactured in718 via crystal plasticity modeling including the role of simulation volume and microstructural constraints," Mater. Sci. Eng. A, 783, 139312 (2020)
[22] K. S. Stopka and D. L. McDowell, "Microstructure-sensitive computational multiaxial fatigue of al 7075-t6 and duplex ti-6al-4v," Int. J. Fatigue, 133, 105460 (2020)
[23] G. M. Castelluccio and D. L. McDowell, "Assessment of small fatigue crack growth driving forces in single crystals with and without slip bands," Int. J. Fract., 176, 49 (2012)
[24] B. D. Smith, D. S. Shih, and D. L. McDowell, "Fatigue hot spot simulation for two widmanstätten titanium microstructures," Int. J. Fatigue, 92, 116 (2016)
[25] B. Chen, J. Jiang, and F. P. E. Dunne, "Is stored energy density the primary meso-scale mechanistic driver for fatigue crack nucleation?," Int. J. Plast., 101, 213 (2018)
[26] T. Gu, K. S. Stopka, C. Xu, and D. L. McDowell, "Prediction of maximum fatigue indicator parameters for duplex ti–6al–4v using extreme value theory," Acta Mater., 188, 504 (2020)
[27] K. S. Stopka, T. Gu, and D. L. McDowell, "Effects of algorithmic simulation parameters on the prediction of extreme value fatigue indicator parameters in duplex ti-6al-4v," Int. J. Fatigue, 141, 105865 (2020)
[28] S. Lucarini and J. Segurado, "An upscaling approach for micromechanics based fatigue: From rves to specimens and component life prediction," Int. J. Fract., 223, 93 (2020)
[29] K. Boyle and W. Curtin, in AIP Conference Proceedings, 2005, vol. 778, no. 1, pp. 433-438: American Institute of Physics.
[30] G. M. Castelluccio and D. L. McDowell, "Microstructure and mesh sensitivities of mesoscale surrogate driving force measures for transgranular fatigue cracks in polycrystals," Mater. Sci. Eng. A, 639, 626 (2015)
[31] M. Diehl, P. Shanthraj, P. Eisenlohr, and F. Roters, "Neighborhood influences on stress and strain partitioning in dual-phase microstructures," Meccanica, 51, 429 (2016)
[32] F. P. E. Dunne and D. Rugg, "On the mechanisms of fatigue facet nucleation in titanium alloys," Fatigue Fract. Eng. Mater. Struct., 31, 949 (2008)
[33] F. P. E. Dunne, D. Rugg, and A. Walker, "Lengthscale-dependent, elastically anisotropic, physically-based hcp crystal plasticity: Application to cold-dwell fatigue in ti alloys," Int. J. Plast., 23, 1061 (2007)
[34] F. P. E. Dunne, A. Walker, and D. Rugg, "A systematic study of hcp crystal orientation and morphology effects in polycrystal deformation and fatigue," Proc. Math. Phys. Eng. Sci., 463, 1467 (2007)
[35] M. Sauzay and T. Jourdan, "Polycrystalline microstructure, cubic elasticity, and nucleation of high-cycle fatigue cracks," Int. J. Fract., 141, 431 (2006)
[36] Y. Kawano, T. Mayama, M. Mitsuhara, S. Yamasaki, and M. Sato, "Generalized slip operation factor considering contribution of secondary slip systems," Mater. Today Commun., 26, 102041 (2021)
[37] Y. Kawano, M. Sato, T. Mayama, M. Mitsuhara, and S. Yamasaki, "Quantitative evaluation of slip activity in polycrystalline α-titanium considering non-local interactions between crystal grains," Int. J. Plast., 127, 102638 (2020)
[38] H. Abdolvand, J. Wright, and A. J. Wilkinson, "Strong grain neighbour effects in polycrystals," Nat. Commun., 9, 171 (2018)
[39] A. Harte, M. Atkinson, M. Preuss, and J. Quinta da Fonseca, "A statistical study of the relationship between plastic strain and lattice misorientation on the surface of a deformed ni-based superalloy," Acta Mater., 195, 555 (2020)

[40] W. D. Musinski, P. A. Shade, D. C. Pagan, and J. V. Bernier, "Statistical aspects of grain-level strain evolution and reorientation during the heating and elastic-plastic loading of a ni-base superalloy at elevated temperature," Materialia, 16, 101063 (2021)
[41] M. Yaghoobi, K. S. Stopka, A. Lakshmanan, V. Sundararaghavan, J. E. Allison, and D. L. McDowell, "Prisms-fatigue computational framework for fatigue analysis in polycrystalline metals and alloys," NPJ Comput. Mater., 7, 38 (2021)
[42] L. K. Aagesen et al., "Prisms: An integrated, open-source framework for accelerating predictive structural materials science," JOM, 70, 2298 (2018)
[43] M. Yaghoobi, J. E. Allison, and V. Sundararaghavan, "Multiscale modeling of twinning and detwinning behavior of hcp polycrystals," Int. J. Plast., 127, 102653 (2020)
[44] S. Ganesan et al., "The effects of heat treatment on the response of we43 mg alloy: Crystal plasticity finite element simulation and sem-dic experiment," Int. J. Plast., 137, 102917 (2021)
[45] B. Puchala, G. Tarcea, E. A. Marquis, M. Hedstrom, H. V. Jagadish, and J. E. Allison, "The materials commons: A collaboration platform and information repository for the global materials community," JOM, 68, 2035 (2016)
[46] M. Yaghoobi, Z. Chen, V. Sundararaghavan, S. Daly, and J. E. Allison, "Crystal plasticity finite element modeling of extension twinning in we43 mg alloys: Calibration and validation," Integr. Mater. Manuf. Innov., 10, 488 (2021)
[47] G. Z. Voyiadjis and M. Yaghoobi, Size effects in plasticity: From macro to nano. Academic Press, 2019.
[48] C. Hennessey, G. M. Castelluccio, and D. L. McDowell, "Sensitivity of polycrystal plasticity to slip system kinematic hardening laws for al 7075-t6," Mater. Sci. Eng. A, 687, 241 (2017)
[49] C. A. Sweeney, B. O'Brien, F. P. E. Dunne, P. E. McHugh, and S. B. Leen, "Strain-gradient modelling of grain size effects on fatigue of cocr alloy," Acta Mater., 78, 341 (2014)
[50] U. Borg, "A strain gradient crystal plasticity analysis of grain size effects in polycrystals," Eur. J. Mech. A Solids, 26, 313 (2007)
[51] M. A. Groeber and M. A. Jackson, "Dream.3d: A digital representation environment for the analysis of microstructure in 3d," Integr. Mater. Manuf. Innov., 3, 56 (2014)
[52] M. Groeber, S. Ghosh, M. D. Uchic, and D. M. Dimiduk, "A framework for automated analysis and simulation of 3d polycrystalline microstructures.: Part 1: Statistical characterization," Acta Mater., 56, 1257 (2008)
[53] M. Groeber, S. Ghosh, M. D. Uchic, and D. M. Dimiduk, "A framework for automated analysis and simulation of 3d polycrystalline microstructures. Part 2: Synthetic structure generation," Acta Mater., 56, 1274 (2008)
[54] D. Naragani et al., "Investigation of fatigue crack initiation from a non-metallic inclusion via high energy x-ray diffraction microscopy," Acta Mater., 137, 71 (2017)
[55] M. D. Sangid, P. Ravi, V. Prithivirajan, N. A. Miller, P. Kenesei, and J.-S. Park, "Icme approach to determining critical pore size of in718 produced by selective laser melting," JOM, 72, 465 (2020)
[56] D. Ozturk, A. Shahba, and S. Ghosh, "Crystal plasticity fe study of the effect of thermo-mechanical loading on fatigue crack nucleation in titanium alloys," Fatigue Fract. Eng. Mater. Struct., 39, 752 (2016)
[57] T. Zhao and Y. Jiang, "Fatigue of 7075-t651 aluminum alloy," Int. J. Fatigue, 30, 834 (2008)
[58] F. J. Humphreys and M. Hatherly, Recrystallization and related annealing phenomena (second edition), F. J. Humphreys and M. Hatherly, Eds. (Oxford: Elsevier, 2004), p. 215.
[59] P. Ramesh Narayanan, S. Suwas, K. Sreekumar, P. P. Sinha, and S. Ranganathan, "Evolution of crystallographic texture in cold rolled al-zn-mg alloys used in space applications," Mater. Sci. Forum, 702-703, 315 (2012)

[60] K. S. Stopka, M. Yaghoobi, J. E. Allison, and D. L. McDowell, "Effects of boundary conditions on microstructure-sensitive fatigue crystal plasticity analysis," Integr. Mater. Manuf. Innov., 10, 393 (2021)
[61] A. Pineau, D. L. McDowell, E. P. Busso, and S. D. Antolovich, "Failure of metals ii: Fatigue," Acta Mater., 107, 484 (2016)
[62] A. Fatemi and D. F. Socie, "A critical plane approach to multiaxial fatigue damage including out-of-phase loading," Fatigue Fract. Eng. Mater. Struct., 11, 149 (1988)
[63] J. E. Bozek et al., "A geometric approach to modeling microstructurally small fatigue crack formation: I. Probabilistic simulation of constituent particle cracking in aa 7075-t651," Modell. Simul. Mater. Sci. Eng., 16, 065007 (2008)
[64] J. D. Hochhalter et al., "A geometric approach to modeling microstructurally small fatigue crack formation: Ii. Physically based modeling of microstructure-dependent slip localization and actuation of the crack nucleation mechanism in aa 7075-t651," Modell. Simul. Mater. Sci. Eng., 18, 045004 (2010)
[65] J. D. Hochhalter et al., "A geometric approach to modeling microstructurally small fatigue crack formation: Iii. Development of a semi-empirical model for nucleation," Modell. Simul. Mater. Sci. Eng., 19, 035008 (2011)
[66] R. Bandyopadhyay and M. D. Sangid, "A probabilistic fatigue framework to enable location-specific lifing for critical thermo-mechanical engineering applications," Integr. Mater. Manuf. Innov., 10, 20 (2021)
[67] E. Castillo, Extreme value theory in engineering. Elsevier Science, 2012.
[68] C. P. Przybyla and D. L. McDowell, "Microstructure-sensitive extreme-value probabilities of high-cycle fatigue for surface vs. Subsurface crack formation in duplex ti–6al–4v," Acta Mater., 60, 293 (2012)
[69] Q. Liu and N. Hansen, "Deformation microstructure and orientation of f.C.C. Crystals," physica status solidi (a), 149, 187 (1995)
[70] C. R. Mischke, "Prediction of stochastic endurance strength," J. Vib. Acoust., 109, 113 (1987)
[71] S. Lucarini and J. Segurado, "On the accuracy of spectral solvers for micromechanics based fatigue modeling," Comput. Mech., 63, 365 (2019)
[72] L. Signor, P. Villechaise, T. Ghidossi, E. Lacoste, M. Gueguen, and S. Courtin, "Influence of local crystallographic configuration on microcrack initiation in fatigued 316ln stainless steel: Experiments and crystal plasticity finite elements simulations," Mater. Sci. Eng. A, 649, 239 (2016)
[73] C. P. Przybyla and D. L. McDowell, "Microstructure-sensitive extreme value probabilities for high cycle fatigue of ni-base superalloy in100," Int. J. Plast., 26, 372 (2010)
[74] M. Oja, K. S. Ravi Chandran, and R. G. Tryon, "Orientation imaging microscopy of fatigue crack formation in waspaloy: Crystallographic conditions for crack nucleation," Int. J. Fatigue, 32, 551 (2010)
[75] D. Montes de Oca Zapiain, A. Shanker, and S. R. Kalidindi, "Convolutional neural networks for the localization of plastic velocity gradient tensor in polycrystalline microstructures," J. Eng. Mater. Technol., 144, 011004 (2021)
[76] N. H. Paulson, M. W. Priddy, D. L. McDowell, and S. R. Kalidindi, "Data-driven reduced-order models for rank-ordering the high cycle fatigue performance of polycrystalline microstructures," Materials & Design, 154, 170 (2018)

Largest microstructure with ~160,000 grains, $(0.625\ \text{mm})^3$:

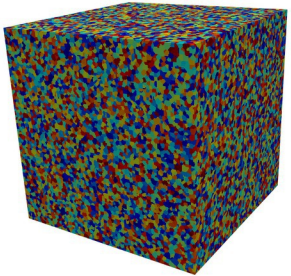

CPFEM

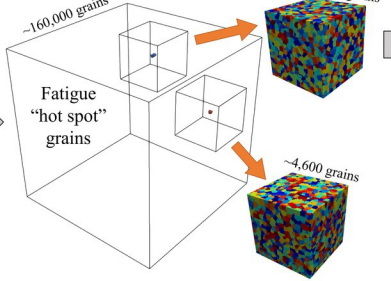

CPFEM

Variability in extreme value
Fatigue Indicator Parameters (FIPs):

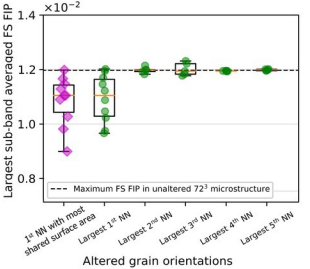

Grain orientations altered in nearest neighbor (NN) layers: